Measurements of ϕ meson production in relativistic heavy-ion collisions at the BNL Relativistic Heavy Ion Collider (RHIC)

B. I. Abelev,[9] M. M. Aggarwal,[30] Z. Ahammed,[46] B. D. Anderson,[19] D. Arkhipkin,[13] G. S. Averichev,[12] Y. Bai,[28] J. Balewski,[23] O. Barannikova,[9] L. S. Barnby,[2] J. Baudot,[17] S. Baumgart,[51] D. R. Beavis,[3] R. Bellwied,[49] F. Benedosso,[28] R. R. Betts,[9] S. Bhardwaj,[35] A. Bhasin,[18] A. K. Bhati,[30] H. Bichsel,[48] J. Bielcik,[11] J. Bielcikova,[11] B. Biritz,[6] L. C. Bland,[3] S.-L. Blyth,[22] M. Bombara,[2] B. E. Bonner,[36] M. Botje,[28] J. Bouchet,[19] E. Braidot,[28] A. V. Brandin,[26] E. Bruna,[51] S. Bueltmann,[3] T. P. Burton,[2] M. Bystersky,[11] X. Z. Cai,[39] H. Caines,[51] M. Calderón de la Barca Sánchez,[5] J. Callner,[9] O. Catu,[51] D. Cebra,[5] R. Cendejas,[6] M. C. Cervantes,[41] Z. Chajecki,[29] P. Chaloupka,[11] S. Chattopadhyay,[46] H. F. Chen,[38] J. H. Chen,[39] J. Y. Chen,[50] J. Cheng,[43] M. Cherney,[10] A. Chikanian,[51] K. E. Choi,[34] W. Christie,[3] S. U. Chung,[3] R. F. Clarke,[41] M. J. M. Codrington,[41] J. P. Coffin,[17] T. M. Cormier,[49] M. R. Cosentino,[37] J. G. Cramer,[48] H. J. Crawford,[4] D. Das,[5] S. Dash,[14] M. Daugherity,[42] C. De Silva,[49] T. G. Dedovich,[12] M. DePhillips,[3] A. A. Derevschikov,[32] R. Derradi de Souza,[7] L. Didenko,[3] P. Djawotho,[16] S. M. Dogra,[18] X. Dong,[22] J. L. Drachenberg,[41] J. E. Draper,[5] F. Du,[51] J. C. Dunlop,[3] M. R. Dutta Mazumdar,[46] W. R. Edwards,[22] L. G. Efimov,[12] E. Elhalhuli,[2] M. Elnimr,[49] V. Emelianov,[26] J. Engelage,[4] G. Eppley,[36] B. Erazmus,[40] M. Estienne,[17] L. Eun,[31] P. Fachini,[3] R. Fatemi,[20] J. Fedorisin,[12] A. Feng,[50] P. Filip,[13] E. Finch,[51] V. Fine,[3] Y. Fisyak,[3] C. A. Gagliardi,[41] L. Gaillard,[2] D. R. Gangadharan,[6] M. S. Ganti,[46] E. Garcia-Solis,[9] V. Ghazikhanian,[6] P. Ghosh,[46] Y. N. Gorbunov,[10] A. Gordon,[3] O. Grebenyuk,[22] D. Grosnick,[45] B. Grube,[34] S. M. Guertin,[6] K. S. F. F. Guimaraes,[37] A. Gupta,[18] N. Gupta,[18] W. Guryn,[3] B. Haag,[5] T. J. Hallman,[3] A. Hamed,[41] J. W. Harris,[51] W. He,[16] M. Heinz,[51] S. Heppelmann,[31] B. Hippolyte,[17] A. Hirsch,[33] A. M. Hoffman,[23] G. W. Hoffmann,[42] D. J. Hofman,[9] R. S. Hollis,[9] H. Z. Huang,[6] T. J. Humanic,[29] G. Igo,[6] A. Iordanova,[9] P. Jacobs,[22] W. W. Jacobs,[16] P. Jakl,[11] F. Jin,[39] P. G. Jones,[2] J. Joseph,[19] E. G. Judd,[4] S. Kabana,[40] K. Kajimoto,[42] K. Kang,[43] J. Kapitan,[11] M. Kaplan,[8] D. Keane,[19] A. Kechechyan,[12] D. Kettler,[48] V. Yu. Khodyrev,[32] J. Kiryluk,[22] A. Kisiel,[29] S. R. Klein,[22] A. G. Knospe,[51] A. Kocoloski,[23] D. D. Koetke,[45] M. Kopytine,[19] L. Kotchenda,[26] V. Kouchpil,[11] P. Kravtsov,[26] V. I. Kravtsov,[32] K. Krueger,[1] M. Krus,[11] C. Kuhn,[17] L. Kumar,[30] P. Kurnadi,[6] M. A. C. Lamont,[3] J. M. Landgraf,[3] S. LaPointe,[49] J. Lauret,[3] A. Lebedev,[3] R. Lednicky,[13] C.-H. Lee,[34] M. J. LeVine,[3] C. Li,[38] Y. Li,[43] G. Lin,[51] X. Lin,[50] S. J. Lindenbaum,[27] M. A. Lisa,[29] F. Liu,[50] H. Liu,[5] J. Liu,[36] L. Liu,[50] T. Ljubicic,[3] W. J. Llope,[36] R. S. Longacre,[3] W. A. Love,[3] Y. Lu,[38] T. Ludlam,[3] D. Lynn,[3] G. L. Ma,[39] J. G. Ma,[6] Y. G. Ma,[39] D. P. Mahapatra,[14] R. Majka,[51] M. I. Mall,[5] L. K. Mangotra,[18] R. Manweiler,[45] S. Margetis,[19] C. Markert,[42] H. S. Matis,[22] Yu. A. Matulenko,[32] T. S. McShane,[10] A. Meschanin,[32] J. Millane,[23] M. L. Miller,[23] N. G. Minaev,[32] S. Mioduszewski,[41] A. Mischke,[28] J. Mitchell,[36] B. Mohanty,[46] D. A. Morozov,[32] M. G. Munhoz,[37] B. K. Nandi,[15] C. Nattrass,[51] T. K. Nayak,[46] J. M. Nelson,[2] C. Nepali,[19] P. K. Netrakanti,[33] M. J. Ng,[4] L. V. Nogach,[32] S. B. Nurushev,[32] G. Odyniec,[22] A. Ogawa,[3] H. Okada,[3] V. Okorokov,[26] D. Olson,[22] M. Pachr,[11] B. S. Page,[16] S. K. Pal,[46] Y. Pandit,[19] Y. Panebratsev,[12] T. Pawlak,[47] T. Peitzmann,[28] V. Perevoztchikov,[3] C. Perkins,[4] W. Peryt,[47] S. C. Phatak,[14] M. Planinic,[52] J. Pluta,[47] N. Poljak,[52] A. M. Poskanzer,[22] B. V. K. S. Potukuchi,[18] D. Prindle,[48] C. Pruneau,[49] N. K. Pruthi,[30] J. Putschke,[51] R. Raniwala,[35] S. Raniwala,[35] R. L. Ray,[42] R. Reed,[5] A. Ridiger,[26] H. G. Ritter,[22] J. B. Roberts,[36] O. V. Rogachevskiy,[12] J. L. Romero,[5] A. Rose,[22] C. Roy,[40] L. Ruan,[3] M. J. Russcher,[28] V. Rykov,[19] R. Sahoo,[40] I. Sakrejda,[22] T. Sakuma,[23] S. Salur,[22] J. Sandweiss,[51] M. Sarsour,[41] J. Schambach,[42] R. P. Scharenberg,[33] N. Schmitz,[24] J. Seger,[10] I. Selyuzhenkov,[16] P. Seyboth,[24] A. Shabetai,[17] E. Shahaliev,[12] M. Shao,[38] M. Sharma,[49] S. S. Shi,[50] X.-H. Shi,[39] E. P. Sichtermann,[22] F. Simon,[24] R. N. Singaraju,[46] M. J. Skoby,[33] N. Smirnov,[51] R. Snellings,[28] P. Sorensen,[3] J. Sowinski,[16] H. M. Spinka,[1] B. Srivastava,[33] A. Stadnik,[12] T. D. S. Stanislaus,[45] D. Staszak,[6] M. Strikhanov,[26] B. Stringfellow,[33] A. A. P. Suaide,[37] M. C. Suarez,[9] N. L. Subba,[19] M. Sumbera,[11] X. M. Sun,[22] Y. Sun,[38] Z. Sun,[21] B. Surrow,[23] T. J. M. Symons,[22] A. Szanto de Toledo,[37] J. Takahashi,[7] A. H. Tang,[3] Z. Tang,[38] T. Tarnowsky,[33] D. Thein,[42] J. H. Thomas,[22] J. Tian,[39] A. R. Timmins,[2] S. Timoshenko,[26] Tlusty ,[11] M. Tokarev,[12] T. A. Trainor,[48] V. N. Tram,[22] A. L. Trattner,[4] S. Trentalange,[6] R. E. Tribble,[41] O. D. Tsai,[6] J. Ulery,[33] T. Ullrich,[3] D. G. Underwood,[1] G. Van Buren,[3] M. van Leeuwen,[28] A. M. Vander Molen,[25] J. A. Vanfossen,[19] R. Varma Jr.,[15] G. M. S. Vasconcelos,[7] I. M. Vasilevski,[13] A. N. Vasiliev,[32] F. Videbaek,[3] S. E. Vigdor,[16] Y. P. Viyogi,[14] S. Vokal,[12] S. A. Voloshin,[49] M. Wada,[42] W. T. Waggoner,[10] F. Wang,[33] G. Wang,[6] J. S. Wang,[21] Q. Wang,[33] X. Wang,[43] X. L. Wang,[38] Y. Wang,[43] J. C. Webb,[45] G. D. Westfall,[25] C. Whitten Jr.,[6] H. Wieman,[22] S. W. Wissink,[16] R. Witt,[44] Y. Wu,[50] N. Xu,[22] Q. H. Xu,[22] Y. Xu,[38] Z. Xu,[3] P. Yepes,[36] I.-K. Yoo,[34] Q. Yue,[43] M. Zawisza,[47] H. Zbroszczyk,[47] W. Zhan,[21] H. Zhang,[3] S. Zhang,[39] W. M. Zhang,[19] Y. Zhang,[38] Z. P. Zhang,[38] Y. Zhao,[38] C. Zhong,[39] J. Zhou,[36] R. Zoulkarneev,[13] Y. Zoulkarneeva,[13] and J. X. Zuo[39]

(STAR Collaboration)

[1]*Argonne National Laboratory, Argonne, Illinois 60439, USA*
[2]*University of Birmingham, Birmingham, United Kingdom*
[3]*Brookhaven National Laboratory, Upton, New York 11973, USA*
[4]*University of California, Berkeley, California 94720, USA*
[5]*University of California, Davis, California 95616, USA*
[6]*University of California, Los Angeles, California 90095, USA*
[7]*Universidade Estadual de Campinas, Sao Paulo, Brazil*
[8]*Carnegie Mellon University, Pittsburgh, Pennsylvania 15213, USA*
[9]*University of Illinois at Chicago, Chicago, Illinois 60607, USA*

[10]*Creighton University, Omaha, Nebraska 68178, USA*
[11]*Nuclear Physics Institute AS CR, CZ-25068 Řež/Prague, Czech Republic*
[12]*Laboratory for High Energy (JINR), Dubna, Russia*
[13]*Particle Physics Laboratory (JINR), Dubna, Russia*
[14]*Institute of Physics, Bhubaneswar 751005, India*
[15]*Indian Institute of Technology, Mumbai, India*
[16]*Indiana University, Bloomington, Indiana 47408, USA*
[17]*Institut de Recherches Subatomiques, Strasbourg, France*
[18]*University of Jammu, Jammu 180001, India*
[19]*Kent State University, Kent, Ohio 44242, USA*
[20]*University of Kentucky, Lexington, Kentucky, 40506-0055, USA*
[21]*Institute of Modern Physics, Lanzhou, People's Republic of China*
[22]*Lawrence Berkeley National Laboratory, Berkeley, California 94720, USA*
[23]*Massachusetts Institute of Technology, Cambridge, Massachusetts 02139-4307, USA*
[24]*Max-Planck-Institut für Physik, Munich, Germany*
[25]*Michigan State University, East Lansing, Michigan 48824, USA*
[26]*Moscow Engineering Physics Institute, Moscow, Russia*
[27]*City College of New York, New York City, New York 10031, USA*
[28]*NIKHEF and Utrecht University, Amsterdam, The Netherlands*
[29]*Ohio State University, Columbus, Ohio 43210, USA*
[30]*Panjab University, Chandigarh 160014, India*
[31]*Pennsylvania State University, University Park, Pennsylvania 16802, USA*
[32]*Institute of High Energy Physics, Protvino, Russia*
[33]*Purdue University, West Lafayette, Indiana 47907, USA*
[34]*Pusan National University, Pusan, Republic of Korea*
[35]*University of Rajasthan, Jaipur 302004, India*
[36]*Rice University, Houston, Texas 77251, USA*
[37]*Universidade de Sao Paulo, Sao Paulo, Brazil*
[38]*University of Science & Technology of China, Hefei 230026, People's Republic of China*
[39]*Shanghai Institute of Applied Physics, Shanghai 201800, People's Republic of China*
[40]*SUBATECH, Nantes, France*
[41]*Texas A&M University, College Station, Texas 77843, USA*
[42]*University of Texas, Austin, Texas 78712, USA*
[43]*Tsinghua University, Beijing 100084, People's Republic of China*
[44]*United States Naval Academy, Annapolis, Maryland 21402, USA*
[45]*Valparaiso University, Valparaiso, Indiana 46383, USA*
[46]*Variable Energy Cyclotron Centre, Kolkata 700064, India*
[47]*Warsaw University of Technology, Warsaw, Poland*
[48]*University of Washington, Seattle, Washington 98195, USA*
[49]*Wayne State University, Detroit, Michigan 48201, USA*
[50]*Institute of Particle Physics, CCNU (HZNU), Wuhan 430079, People's Republic of China*
[51]*Yale University, New Haven, Connecticut 06520, USA*
[52]*University of Zagreb, Zagreb, HR-10002, Croatia*

(Received 17 September 2008; published 15 June 2009)

We present results for the measurement of ϕ meson production via its charged kaon decay channel $\phi \to K^+K^-$ in Au + Au collisions at $\sqrt{s_{NN}} = 62.4, 130$, and 200 GeV, and in $p + p$ and $d +$ Au collisions at $\sqrt{s_{NN}} =$ 200 GeV from the STAR experiment at the BNL Relativistic Heavy Ion Collider (RHIC). The midrapidity ($|y| < 0.5$) ϕ meson transverse momentum (p_T) spectra in central Au + Au collisions are found to be well described by a single exponential distribution. On the other hand, the p_T spectra from $p + p, d +$ Au, and peripheral Au + Au collisions show power-law tails at intermediate and high p_T and are described better by Levy distributions. The constant ϕ/K^- yield ratio vs beam species, collision centrality, and colliding energy is in contradiction with expectations from models having kaon coalescence as the dominant mechanism for ϕ production at RHIC. The Ω/ϕ yield ratio as a function of p_T is consistent with a model based on the recombination of thermal s quarks up to $p_T \sim 4$ GeV/c, but disagrees at higher transverse momenta. The measured nuclear modification factor, $R_{d\mathrm{Au}}$, for the ϕ meson increases above unity at intermediate p_T, similar to that for pions and protons, while R_{AA} is suppressed due to the energy loss effect in central Au + Au collisions. Number of constituent quark scaling of both R_{cp} and v_2 for the ϕ meson with respect to other hadrons in Au + Au collisions

at $\sqrt{s_{NN}} = 200$ GeV at intermediate p_T is observed. These observations support quark coalescence as being the dominant mechanism of hadronization in the intermediate p_T region at RHIC.

DOI: 10.1103/PhysRevC.79.064903 PACS number(s): 25.75.Dw

I. INTRODUCTION

The $\phi(1020)$ vector meson's properties and its transport in the nuclear medium have been of interest since its discovery [1]. The proper lifetime of the ϕ meson is about 45 fm/c, and it decays into charged kaons K^+K^- with a branching ratio of 49.2%, and more rarely into the dilepton pairs e^+e^- (B.R. of 2.97×10^{-4}) and $\mu^+\mu^-$ (B.R. of 2.86×10^{-4}).

The mechanism for ϕ meson production in high energy collisions has remained an open issue. As the lightest bound state of strange quarks ($s\bar{s}$) with hidden strangeness, ϕ meson production is suppressed in elementary collisions because of the Okubo-Zweig-Iizuka (OZI) rule [2–4]. The OZI rule states that processes with disconnected quark lines in the initial and final state are suppressed. In an environment with many strange quarks, ϕ mesons can be produced readily through coalescence, bypassing the OZI rule [5]. The ϕ meson has been predicted to be a probe of the quark-gluon plasma (QGP) formed in ultrarelativistic heavy-ion collisions [6–11].

On the other hand, a naive interpretation of ϕ meson enhancement in heavy-ion collisions would be that the ϕ meson is produced via $K\bar{K} \rightarrow \phi$ in the hadronic rescattering stage. Models that include hadronic rescatterings such as RQMD [12] and UrQMD [13] have predicted an increase of the ϕ to K^- production ratio at midrapidity as a function of the number of participant nucleons. This prediction was disproved in Au + Au collisions at $\sqrt{s_{NN}} = 200$ GeV, from STAR year 2001 data [14]. With the higher statistics data newly recorded from the Solenoidal Tracker at RHIC (STAR) experiment [15], a precise measurement of the ϕ/K^- ratio as a function of beam energy and collision centrality is presented to confirm this finding in this paper.

The in-medium properties of vector mesons in the hot and dense environment are also interesting [11]. The mass and width of the ϕ meson were predicted to change because of the partial restoration of chiral symmetry in the nuclear medium. Asakawa and Ko [16] and Song [17] predicted that the ϕ mass decreases as a result of many-body effects in a hadronic medium. A double ϕ peak structure in the dilepton invariant mass spectrum from relativistic heavy-ion collisions was proposed as a signature of a phase transition from the QGP to hadronic matter [18]. Other calculations have predicted that the ϕ meson width can be widened significantly due to nuclear medium effects [19–21]. Recently, an interesting ϕ mass modification at normal nuclear density in 12 GeV $p + A$ interactions was observed in the dilepton channel ($e^+ + e^-$) from the KEK experiment [22,23]. In STAR, we measure the ϕ meson mass and width to compare with these predictions/measurements, using the decay channel $\phi \rightarrow K^+K^-$.

From phenomenological analysis, it is suggested that the ϕ meson mean free path in hadronic media is large because of its small cross section of scattering with hadrons [5]. Many other calculations also indicate that the ϕ meson has small rescattering cross sections with hadronic matter [19,20]. However, after including three- and four-vector meson vertices into their hidden local symmetry model, Alvarez-Ruso and Koch [24] found that the ϕ meson mean free path in nuclear media is smaller than that usually estimated. Ishikawa *et al.* [25] presented new data on near-threshold ϕ photoproduction on several nuclear targets. They found that the cross section between a ϕ meson and a nucleon, $\sigma_{\phi N}$, is equal to 35^{+17}_{-11} mb, which appears to be much larger than previous expectations, although the experimental uncertainty is very large [26]. Meanwhile, Sibirtsev *et al.* [27] presented a new analysis of existing ϕ photoproduction data and found $\sigma_{\phi N} \sim 10$ mb. Thus, $\sigma_{\phi N}$ in heavy-ion collisions is still unclear.

The measurement of collective radial flow (represented by $\langle p_T \rangle$) probes the equation of state of matter produced in nuclear collisions [28,29]. Strong radial flow has been observed for many particles such as π, K, and $p(\bar{p})$ [30]. If the ϕ meson has indeed small hadronic rescattering cross sections and decouples early from the collision system, contributions to the radial flow of the ϕ meson will be mostly from the partonic stage instead of the hadronic stage. Thus the ϕ meson may have a significantly smaller radial flow than other hadrons with similar mass, such as the proton, especially in central heavy-ion collisions. Therefore, ϕ mesons may carry information about the conditions of nuclear collisions before chemical freeze-out. Thus it is important to experimentally measure and compare the freeze-out properties of the ϕ to other hadrons as a function of centrality and collision species. A comprehensive set of measurements will shed light on the characteristics of ϕ meson production and the evolution of the collision system.

The elliptic flow parameter v_2 is a good tool for studying the system formed in the early stages of high energy collisions at RHIC. It has been found that at low p_T ($0 < p_T < 2$ GeV/c), the dependence of v_2 on particle mass [31–33] is consistent with hydrodynamic calculations in which local thermal equilibrium of partons is assumed [34–38]. This observation indicates that thermally equilibrated partonic matter may have been created at RHIC. However, at intermediate p_T ($2 < p_T < 5$ GeV/c), the measured v_2 for various hadrons seems to depend on the number of constituent quarks in the hadron rather than its mass, consistent with the results from coalescence/recombination models [39–44]. Since ϕ is a meson but has a mass close to that of the proton and Λ, the measurement of the ϕ meson elliptic flow will provide a unique tool for testing the above statement.

Current measurements of various hadrons by STAR (Λ, p, K^0_S, $K(892)^*$, $h^{\pm}$, etc.) show that the nuclear modification factor $R_{\rm cp}$ for baryons differs from that of mesons [45,46], consistent with the prediction of quark coalescence/recombination models [42,43,47,48]. Because of the value of the ϕ meson mass, a comparison of $R_{\rm cp}$ for the ϕ with these previous measurements will conclusively determine if the observed difference is driven by particle mass or particle type.

In previous studies, the production of the ϕ meson has been measured in Au + Au collisions at $\sqrt{s_{NN}} = 130$ GeV [49] and in Au + Au and $p + p$ collisions at $\sqrt{s_{NN}} =$ 200 GeV [14] at RHIC. The Au + Au 200 GeV data presented in this paper were taken from the year 2004 run, where the number of events is approximately ten times larger than the previously reported number for the Au + Au run in year 2001 [14]. The data from the year 2004 run contain the data reported in Refs. [50,51]. It has been found that the results from the two runs are consistent with each other. In this paper, we present systematic measurements of ϕ meson production over a broad range of collision energies and system sizes, including Au + Au collisions at $\sqrt{s_{NN}} = 62.4$, 130 [49], and 200 GeV, and $p + p$ [14] and d + Au collisions at $\sqrt{s_{NN}} = 200$ GeV from the STAR experiment. In Sec. II, we briefly introduce the STAR detector and discuss our analysis method (event-mixing technique) in detail. In Sec. III, we present the measurement of ϕ meson invariant mass distributions (III A), transverse mass m_T spectra (III B), particle ratios (III C), nuclear modification factors (III D), and the elliptic flow parameter v_2 (III E); we also discuss the physics implication of each of these results. A summary and conclusions are presented in Sec. IV.

II. DATA ANALYSIS

A. Experimental setup

The STAR detector [15] consists of several subsystems in a large solenoidal analyzing magnet. We discuss here the subdetectors used in the analyses relevant to this paper. With its axis aligned along the beam direction, the time projection chamber (TPC) [52] is the main tracking device for charged particles, covering a pseudorapidity range $|\eta| \leqslant 1.8$ and providing complete azimuthal coverage. The entire TPC is located inside a solenoidal magnet, and data are taken at the maximum magnetic field $|B_z| = 0.5$ Tesla, where the z axis is parallel to the beam direction. Radial-drift TPCs (FTPCs) [53] are also installed to extend particle tracking into the forward and backward regions ($2.5 < |\eta| < 4.0$). Surrounding the TPC is the central trigger barrel (CTB) [54], which is a scintillator counter array whose analog signal is sensitive to the total charged particle multiplicity with coverage $|\eta| \leqslant 1.0$. A pair of beam-beam counters (BBCs) at $3.3 < \eta < 5.0$ and a pair of zero degree calorimeters (ZDCs) [55] at $\theta < 2$ mrad are located on either side of the collision region along the beam line, and are used to provide event triggers for data taking. A more detailed description of the STAR detector can be found in Ref. [15] and references therein.

B. Event selection

1. Trigger selection

The Au + Au data used in this analysis were taken with two different trigger conditions. One was a minimum-bias (MB) trigger requiring only a coincidence between both ZDCs. The other was a central trigger additionally requiring both a large analog signal in the CTB indicating a high charged particle multiplicity at midrapidity and a small ZDC signal. The ZDCs measure beam-velocity neutrons from the fragmentation of colliding nuclei and were used as the experimental level-0 trigger for selecting d + Au and Au + Au collisions for their respective runs. For $p + p$ data taking, the BBCs were used as trigger detectors. The central trigger corresponds to approximately the top 15% and 12% of the measured cross section for Au + Au collisions at 130 GeV and 200 GeV, respectively. Data from both the MB and central triggers were used for this analysis. For the Au + Au 62.4 GeV data set, only MB triggered events were used. For $p + p$ collisions at 200 GeV, the MB trigger was used in the analysis. It was based on a coincidence between the two BBCs. The BBCs are sensitive only to the non-single diffractive (NSD) part (30 mb) of the $p + p$ total inelastic cross section (42 mb) [14].

2. Vertex cuts and centrality selection

The longitudinal z position of the interaction point is determined on-line by the measured time difference of the two ZDCs's signals. A cut on the z position of the interaction point is applied on-line for all data sets (except $p + p$) in order to maximize the amount of useful data for physics analysis, since events with primary vertices far away from the center of the TPC have a significant non-uniform acceptance. In the off-line data analysis further cuts are applied on the z position of the reconstructed primary vertex (V_Z), to ensure nearly uniform detector acceptance. These cuts are listed in Table I.

To define the collision centrality for the Au + Au data, the raw charged hadron multiplicity distribution in the TPC within a pseudorapidity window $|\eta| \leqslant 0.5$ ($|\eta| \leqslant 0.75$ was used for the Au + Au 130 GeV data) was divided into several bins. Each bin corresponds to a certain fraction of the total inelastic cross section [56]. For the d + Au data, the raw charged hadron multiplicity in the east (Au-direction) FTPC ($-3.8 < \eta < -2.8$) was used for the centrality definition to avoid auto-correlation between centrality and the measurements of charged particles at midrapidity in the TPC [56]. We defined four centrality bins for the Au + Au 62.4 GeV data (0–20%, 20–40%, 40–60%, 60–80%), three centrality bins for the Au + Au 130 GeV data (0–11%, 11–26%, 26–85%), nine centrality bins for the Au + Au 200 GeV data (0–5%, 0–10%, 10–20%, 20–30%, 30–40%, 40–50%, 50–60%, 60–70%, 70–80%) and three centrality bins for the d + Au 200 GeV data (0–20%, 20–40%, 40–100%). The 80–100% most peripheral Au + Au collision data were not used because of the rapidly decreasing trigger and vertex finding efficiencies

TABLE I. Data sets used in the analysis. Cuts on V_Z, the selected centrality ranges, and the final number of events included in the analysis after all cuts/selections are also shown.

System	$\sqrt{s_{NN}}$ (GeV)	Trigger	$\lvert V_Z\rvert$ (cm)	Centrality	Events	Year
Au + Au	62.4	MB	$\leqslant 30$	0–80%	6.2×10^6	2004
Au + Au	130	MB	$\leqslant 80$	0–85%	7.6×10^5	2000
Au + Au	130	Central	$\leqslant 80$	0–11%	8.8×10^5	2000
Au + Au	200	MB	$\leqslant 30$	0–80%	1.4×10^7	2004
Au + Au	200	Central	$\leqslant 30$	0–5%	4.8×10^6	2004
$p + p$	200	MB	$\leqslant 50$	MB (NSD)	6.5×10^6	2002
d + Au	200	MB	$\leqslant 50$	MB	1.4×10^7	2003

for low multiplicity events. Table I lists the data sets used along with centrality selections and final numbers of events after these cuts. Note that the elliptic flow v_2 measurement only from 200 GeV MB Au + Au data is presented in this paper, as the statistics for the v_2 analysis is not sufficient for the 62.4 and 130 GeV Au + Au data.

C. Track selection and particle identification

1. Track selection

Several quality cuts were applied to ensure selection of good tracks. During the TPC track reconstruction, a charged track was extrapolated back to the beam line by using the reconstructed helix parameters. If the distance of closest approach (DCA) of the track to the event vertex was less than 3 cm and the track had at least ten hit points in the TPC, the reconstructed track was labeled as a primary track. The helix parameters for primary tracks were then refitted by requiring that the helix pass through the primary vertex location. This procedure improved the momentum resolution of tracks. Since the ϕ meson has a very short lifetime, it decays at the primary vertex position. Thus only primary tracks were used for the ϕ meson analysis. As a systematic check, the DCA selection for primary tracks was changed from 3 cm to 1 cm. The differences in the results were small and were included in the estimate of systematic uncertainties. Tracks with transverse momentum less than 0.1 GeV/c were not used, as their combined acceptance and efficiency becomes very small. Each track included in the ϕ analysis was required to have at least 15 hit points out of 45 used in the fitting of the tracks helix parameters. The ratio of the number of space points used in the track reconstruction to the maximum possible number of hit points was required to be greater than 55% to avoid split tracks where a real track is reconstructed in two or more segments. A pseudorapidity cut $|\eta| < 1.0$ ($|\eta| < 1.1$ for Au + Au 130 GeV data) was applied to select tracks that are well within the TPC acceptance.

2. Kaon selection

Particle identification (PID) was achieved by correlating the ionization energy loss (dE/dx) of charged particles in the TPC gas with their measured momentum. The measurement of mean dE/dx was achieved by averaging the measured dE/dx samples along the track after truncating the top 30%. The measured $\langle dE/dx\rangle$ versus momentum curve is reasonably well described by the Bethe-Bloch function [57] smeared with the detector's resolution (note that the Bichsel function was used to fit the $\langle dE/dx\rangle$ plot in Au + Au 200 GeV from the year 2004 run [58]). The n_σ values for kaons are calculated via

$$n_\sigma = \frac{1}{R}\log\frac{\langle dE/dx\rangle_{\text{measured}}}{dE/dx_{\text{expected}}}, \qquad (1)$$

where $\langle dE/dx\rangle_{\text{measured}}$ and dE/dx_{expected} are $\langle dE/dx\rangle$ measured by TPC and calculated analytically, respectively, and R denotes the dE/dx resolution of the track which is found to range between 6% and 10%. R is determined experimentally and depends on the event multiplicity and the number of dE/dx samples from the track used to calculate the mean value. Tracks within 2σ of the kaon Bethe-Bloch curve were selected as kaon candidates. Figure 1 presents the measured $\langle dE/dx\rangle$ versus momentum × charge in Au + Au collisions at 62.4 GeV. Table II lists all the track cuts applied in the analysis.

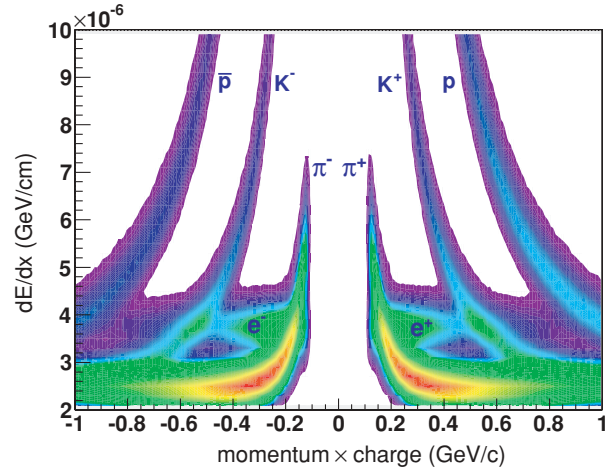

FIG. 1. (Color online) Measured $\langle dE/dx\rangle$ vs momentum × charge of reconstructed tracks in the TPC. The figure is generated from Au + Au 62.4 GeV data.

Note that from the $\langle dE/dx\rangle$ measurement, kaons cannot be clearly separated from pions above $p \sim 0.6$ GeV/c and from protons/antiprotons above $p \sim 1.1$ GeV/c. Also note that the electron and positron dE/dx bands cross the bands for pions, kaons, and protons/antiprotons. Therefore selected kaon candidates are contaminated by electrons/positrons, pions, and protons/antiprotons varying with p. Contamination by these charged particles in the kaon sample brings in additional real correlations (such as particle decays) which cannot be subtracted by the event-mixing method. We have varied the n_σ cut for kaon to investigate the efficiency and combinatorial background dependence of the ϕ signal extraction on this cut. The resulting systematic uncertainties have been included in the estimate of the total systematic errors.

TABLE II. Track cuts used in the analysis, where N_{Fit} and N_{Max} represent the number of fitted hits and the maximum number of hits for TPC tracks, respectively.

Cut parameter	Value
Track DCA (cm)	<3
Track N_{Fit}	$\geqslant$15
Track $N_{\text{Fit}}/N_{\text{Max}}$	>0.55
Track momentum (GeV/c)	$0.1 < p < 10$
Track transverse momentum (GeV/c)	$0.1 < p_T < 10$
Kaon dE/dx	$\lvert n_\sigma\rvert < 2.0$ (for kaon)
ϕ candidate's δ-dip-angle (radians)	>0.04
ϕ candidate's rapidity	$\lvert y\rvert < 0.5$ (for spectra) $\lvert y\rvert < 1.0$ (for v_2)

D. Event mixing and raw yield extraction

The ϕ meson signal was generated by pairing all K^+K^- tracks from the same event that passed the selection criteria and by then calculating the invariant mass $m_{\rm inv}$ for all possible K^+K^- pairs. As random combinations of K^+K^- pairs are dominant in this process, the resulting same-event invariant mass distribution contains the ϕ meson signal on top of a large combinatorial background. An event-mixing technique [59,60] was applied to calculate the shape of the combinatorial background, where the invariant mass was calculated by pairing two kaons from two different events with same primary vertex and multiplicity bins (mixed event). Ideally, since it combines two different events, the mixed-event distribution contains everything except the real same-event correlations.

The STAR TPC has symmetric coverage about the center of the collision region. However, variations in the acceptance occur, since the collision vertex position may change considerably event-by-event. This variation in the collision vertex position gives rise to a nonstatistical variation in the single-particle phase-space acceptance, which would lead to a mismatch between the mixed-event and same-event invariant mass distributions. This mismatch would prevent the proper extraction of the ϕ meson signal. By sorting events according to their primary vertex V_Z position and performing event-mixing only among events in the same vertex bin, the mismatching effect is minimized. In this analysis, events were divided into V_Z bins that were 6 cm wide (V_Z resolution is $\sim$0.3 mm) for event-mixing. To further improve the description of the background, two events were only mixed if they had similar event multiplicities. These requirements ensure that the two events used in mixing have similar event structures, so the mixed-event invariant mass distribution can better represent the combinatorial background in the same-event invariant mass distribution. Consistent results were obtained when we constructed the background distribution using like-sign pairs from the same event.

To reduce statistical uncertainty in the mixed event, each event was mixed with five to ten other events (depending on the collision system). To extract the ϕ meson signal, the mixed-event and same-event K^+K^- invariant mass distributions were accumulated, and the mixed-event distribution normalized to the same-event distribution in the region above the ϕ mass, $1.04 < m_{\rm inv} < 1.06$ GeV/c^2, and subtracted in each p_T and y (rapidity) bin for every collision centrality. We varied the normalization region and normalization factor to estimate the systematic uncertainty on the normalization, and the estimated uncertainty was included in the quoted total systematic uncertainty.

Despite the requirements for mixing events described above, a residual background remains over a broad mass region in the subtracted invariant mass distribution. This is due to an imperfect description of the combinatorial background and the fact that the mixed event cannot account for the real correlated background from decay pairs due to Coulomb interactions, photon conversions ($\gamma \to e^+e^-$), and particle decays such as $K^{0*} \to K^+\pi^-$, $\rho^0 \to \pi^+\pi^-$, $K^0_S \to \pi^+\pi^-$, and $\Lambda \to p\pi^-$ [61]. For example, when both pions from a K^0_S decay are misidentified as kaons, the real correlation from decay will remain in the same-event as a broad distribution but will not be reproduced by the event-mixing method.

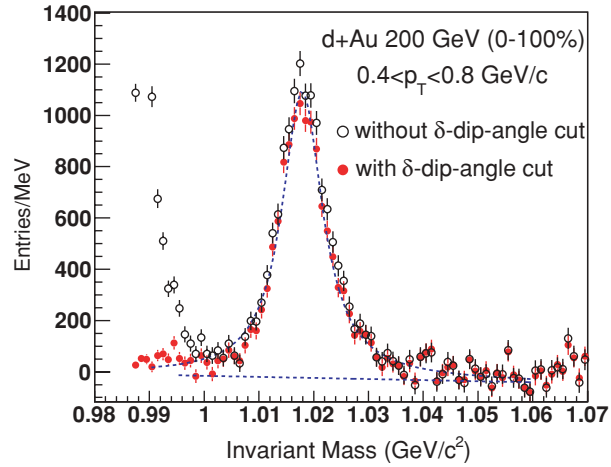

FIG. 2. (Color online) Background-subtracted invariant mass distributions at $0.4 < p_T < 0.8$ GeV/c in d + Au 200 GeV collisions (0–100%) with (solid points) and without (open points) the δ-dip-angle cut. The dashed curves show a Breit-Wigner (see the text for details) + linear background function fit to the case with the δ-dip-angle cut.

Because of contamination of electrons/positrons in the selected kaon sample, the K^+K^- invariant mass distribution contains residual background near the threshold from correlated e^+e^- pairs, mainly from photon conversions ($\gamma \to e^+ + e^-$). The δ-dip-angle between the photon converted electron and positron is usually quite small. The δ-dip-angle is calculated from

$$\delta\text{-dip-angle} = \cos^{-1}\left[\frac{p_{T1}p_{T2} + p_{z1}p_{z2}}{p_1 p_2}\right], \qquad (2)$$

where p_1, p_2, p_{T1}, p_{T2}, p_{z1}, p_{z2} are momentum and transverse and longitudinal momentum components of the two tracks; this represents the opening angle of a pair in the p_z-p_T plane. We required the δ-dip-angle to be greater than 0.04 radians. This cut was found to be very effective in removing the photon conversion background while only reducing the ϕ reconstruction efficiency by $\sim$12%. Figure 2 shows two background-subtracted invariant mass distributions with and without the δ-dip-angle cut. One can see that the peak from photon conversion ($m_{\rm inv} \leqslant 1.0$ GeV/c^2) is very effectively removed by this cut.

Figure 3 shows the K^+K^- invariant mass distributions for $p + p$ collisions at 200 GeV [(a) and (b)], 60–80% Au + Au collisions at 62.4 GeV [(c) and (d)], and 0–10% Au + Au collisions at 200 GeV [(e) and (f)]. Solid circles in the upper panels are same-event pairs, whereas the histograms are from mixed-event pairs. The ϕ meson peak is clearly visible for $p + p$ 200 GeV and Au + Au 62.4 GeV (60–80%) in Figs. 3(a) and 3(c) before background subtraction, but not for Au + Au 200 GeV (0–10%) [Fig. 3(e)] due to its smaller signal significance. However, after background subtraction, the ϕ mass peak can be seen clearly for all data sets. The lower panels in Fig. 3 show the mixed-event background-subtracted ϕ invariant mass distributions. Raw yields for the ϕ meson

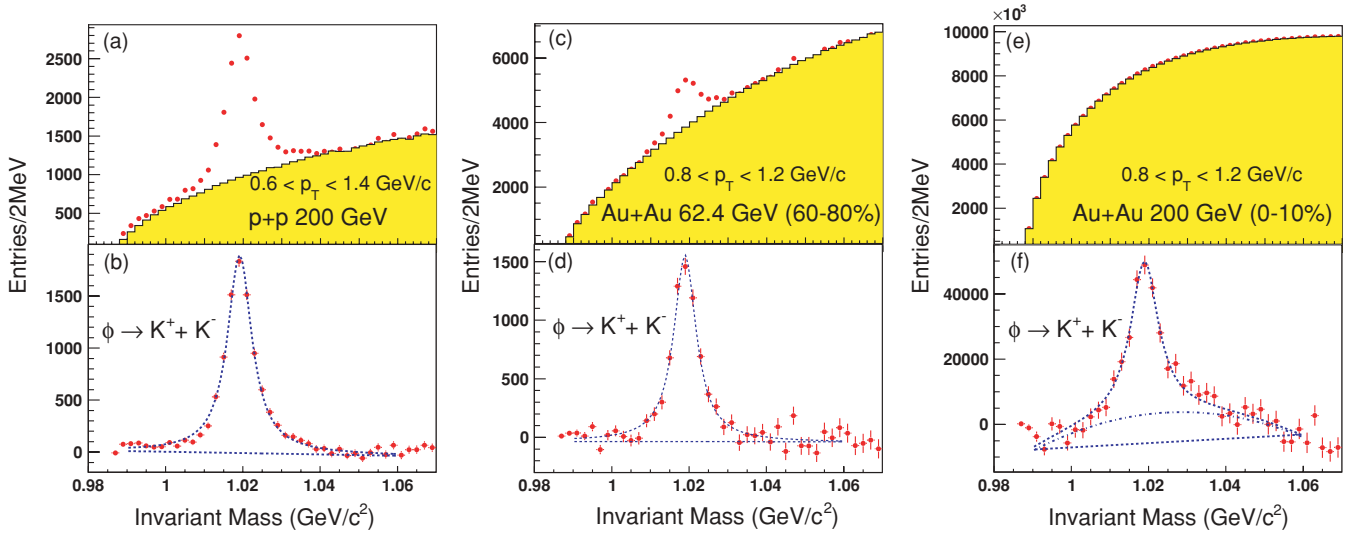

FIG. 3. (Color online) Upper panels: same-event (full points) and mixed-event (solid line) K^+K^- invariant mass distributions at $0.6 < p_T < 1.4$ GeV/c in $p + p$ 200 GeV collisions (a), $0.8 < p_T < 1.2$ GeV/c in Au + Au 62.4 GeV collisions (60–80%) (c), and $0.8 < p_T < 1.2$ GeV/c in Au + Au 200 GeV collisions (0–10%) (e). Lower panels: the corresponding ϕ meson mass peaks after subtracting the background. Dashed curves show a Breit-Wigner + linear background function fit in (b), (d). In (f), both linear and quadratic backgrounds are shown as dashed and dot-dashed lines, respectively.

were determined by fitting the background-subtracted $m_{\rm inv}$ distribution with a Breit-Wigner function superimposed on a linear (or polynomial) background function

$$\frac{dN}{dm_{\rm inv}} = \frac{A\Gamma}{(m_{\rm inv} - m_0)^2 + \Gamma^2/4} + B(m_{\rm inv}), \qquad (3)$$

where A is the area under the peak corresponding to the number of ϕ mesons, Γ is the full width at half maximum (FWHM) of the peak, and m_0 is the resonance mass position. $B(m_{\rm inv})$ denotes a linear [$B(m_{\rm inv}) = p_0 + p_1 m_{\rm inv}$, shown by a dashed line in Figs. 3(b), 3(d) and 3(f)] or polynomial [$B(m_{\rm inv}) = p_0 + p_1 m_{\rm inv} + p_2 m_{\rm inv}^2$, shown by a dot-dashed line in Fig. 3(f)] residual background function. The parameters p_0, p_1, and p_2 of $B(m_{\rm inv})$ and A, m_0, and Γ are free parameters.

E. Efficiency correction

The ϕ acceptance and reconstruction efficiency were calculated using an embedding technique, in which simulated tracks were embedded into real events. The number of embedded simulated tracks is approximately 5% of the measured multiplicity of the real event. The ϕ meson decay ($\phi \to K^+K^-$) and the detector responses were simulated by the GEANT program package [62] and the simulated output signals were embedded into real events before being processed by the standard STAR event reconstruction code. Embedded data were then analyzed to calculate tracking efficiencies and detector acceptance by dividing the number of reconstructed ϕ by the number of input ϕ in the desired kinematic regions. Figure 4 shows examples of correction factors (tracking efficiency × acceptance) for our analysis as a function of ϕ meson p_T for selected centrality bins for Au + Au, d + Au, and $p + p$ 200 GeV collisions. It can be seen that the overall correction factors increase from a few percent at low p_T to over 30% at high p_T. Low efficiency at low p_T is mainly due to poor acceptance of the daughter tracks. The efficiency is lower in more central collisions because of the increasing occupancy in the TPC [56].

F. Vertex finding and trigger efficiency correction

For $p + p$ and d + Au data, the trigger efficiency is less than 100% [63]. The MB trigger for $p + p$ data was found to trigger ∼87% of $p + p$ NSD events. For d + Au data, the trigger efficiency was found to be ∼95%. These trigger efficiencies were used to normalize the measured yield, and the corresponding uncertainties are added to the total systematic

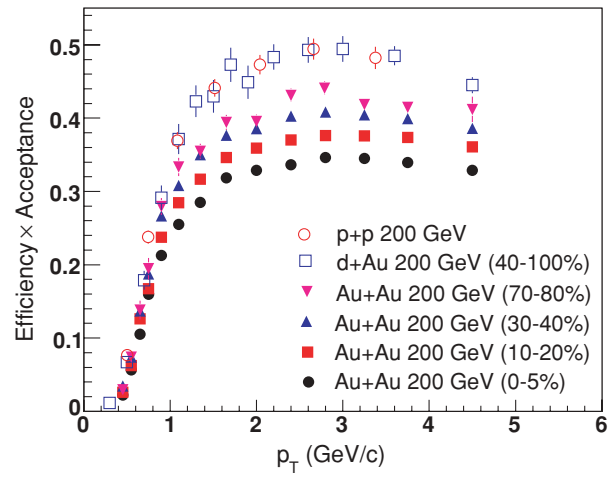

FIG. 4. (Color online) Reconstruction efficiency including acceptance of ϕ meson as a function of p_T in several centrality bins of Au + Au, d + Au, and $p + p$ 200 GeV collisions.

errors for $p + p$ and $d + \mathrm{Au}$ data. The MB trigger efficiency for Au + Au data is essentially 100% [56].

It was found that the event vertex finding efficiency, which is the fraction of events having reconstructed vertices, drops rapidly for low multiplicity events [56]. For $d + \mathrm{Au}$ collisions, the vertex efficiency was 88% for the most peripheral bin (40–100%), 93% for the MB events, and 100% for the central and middle central bins (0–20% and 20–40%). For Au + Au collisions, the vertex finding efficiency was 99.9% and p_T independent [64] due to the increased track multiplicity in those collisions. However, the overall vertex finding efficiency was found to be 98.8% for the MB $p + p$ data by applying an additional BBC time difference selection (i.e., the NSD requirement), and the effect of correction was negligible in this analysis.

G. v_2 measurement

1. Reaction plane method

We employed the STAR standard reaction plane method as described in Refs. [65,66], which uses a Fourier expansion to describe particle emission with respect to the reaction plane angle, that is,

$$E\frac{d^3N}{d^3p} = \frac{1}{2\pi}\frac{d^2N}{p_t\,dp_t\,dy}\left(1 + \sum_{n=1}^{\infty} 2v_n \cos[n(\varphi - \Psi_r)]\right), \quad (4)$$

where Ψ_r is the real reaction plane angle and φ is the particle's azimuthal angle. The coefficient v_2 in the second-order term of the expansion is the dominant part and is called the second harmonic anisotropic flow parameter, or elliptic flow.

The real reaction plane angle Ψ_r is not known but can be estimated experimentally [67]. In our analysis, the estimated reaction plane angle from the second-order harmonic (Ψ_2) was used. This has a finite resolution due to a limited number of particles available in each event and a different event-by-event v_2, which is used for the estimation. The estimated reaction plane resolution was used to correct the observed v_2^{obs} to obtain the final estimation of v_2.

The event plane angle Ψ_2 was calculated by the equation

$$\Psi_2 = \frac{1}{2}\tan^{-1}\left(\frac{\sum_i w_i \sin(2\varphi_i)}{\sum_i w_i \cos(2\varphi_i)}\right), \quad (5)$$

where the sums are over all charged particles used for reaction plane determination, and w_i and φ_i are the weight and azimuthal angle for the ith particle in a given event, respectively. The weights include both a p_T weight and φ weight. The p_T weight was taken to be the particle p_T up to 2.0 GeV/c and constant (2.0) above that [66]. The φ weight was taken to be the reciprocal of the φ distribution (normalized by the average entries) for all selected tracks. The autocorrelations were eliminated by excluding all kaon tracks used in the ϕ invariant mass calculation from the reaction plane angle estimation [64].

The reaction plane resolution was then calculated by

$$\langle \cos[2(\Psi_2 - \Psi_r)]\rangle = C\langle \cos\left[2\left(\Psi_2^a - \Psi_r\right)\right]\rangle, \quad (6)$$

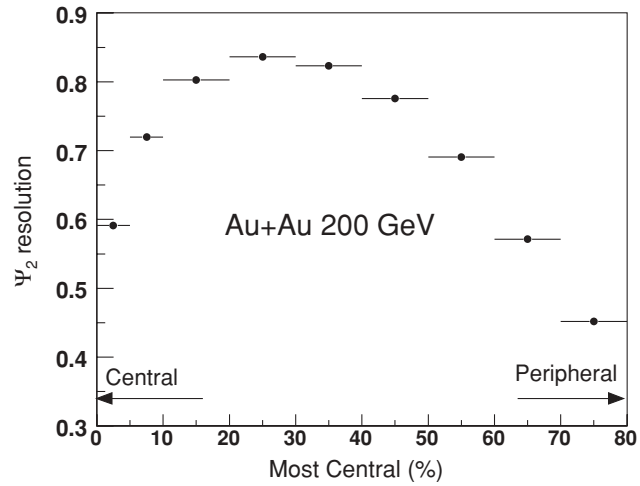

FIG. 5. Event plane Ψ_2 resolution as a function of centrality in Au + Au 200 GeV collisions, where the vertical axis starts from 0.3 for clarity.

where Ψ_2^a is the calculated reaction plane angle of the subevent, and C is a constant calculated from the known multiplicity dependence of the resolution [66]. This resolution was determined by dividing each event into two random subevents, a and b, with equal multiplicities. The reaction plane resolution therefore corresponds to how accurately the event plane angle represents the real reaction plane; due to its the definition in Eq. (6), a value of unity indicates ideal resolution. Figure 5 presents the reaction plane resolutions in different centrality bins for Au + Au 200 GeV collisions.

The combinatorial background in the ϕ invariant mass distribution was also calculated by an event-mixing technique as described above. To guarantee the mixed-event sample would represent the combinatorial background, an additional cut, the reaction plane angle difference between two mixed events, was required to be less than 0.1π rad in the event-mixing procedure. After background subtraction, the ϕ meson yield was extracted in each $(p_T, \varphi - \Psi_2)$ bin. The yield distribution as a function of $\varphi - \Psi_2$ was fitted by the function

$$A\left(1 + 2v_2^{\mathrm{obs}}\cos[2(\varphi - \Psi_2)]\right), \quad (7)$$

to extract the v_2^{obs} value, where A is a constant. A typical result for the Au + Au data at 200 GeV is presented in Fig. 6.

The measured v_2^{obs} was then divided by the reaction plane resolution to obtain the final v_2, i.e.,

$$v_2 = \frac{v_2^{\mathrm{obs}}}{\langle \cos[2(\Psi_2 - \Psi_r)]\rangle}. \quad (8)$$

Simulation studies have found that the measured v_2 is about 7% (relative to the real v_2) lower than the real v_2 due to binning effects (five bins in $\varphi - \Psi_2$); a correction has been made to the measured v_2 to account for this effect.

2. Invariant mass method

A new method, namely, the *invariant mass method*, was also used to extract the elliptic flow v_2 of the ϕ meson. The method was proposed in Ref. [68], which decomposes the

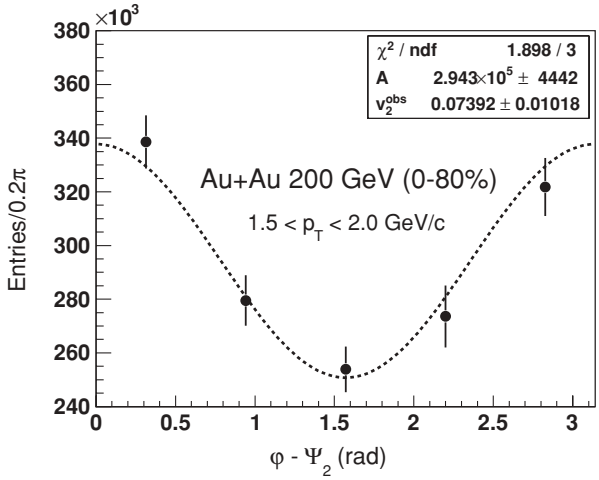

FIG. 6. $\varphi - \Psi_2$ distribution for ϕ meson at $1.5 < p_T < 2.0$ GeV/c in Au + Au collisions (0–80%) at 200 GeV. The line is the fitting result. Error bars are statistical only.

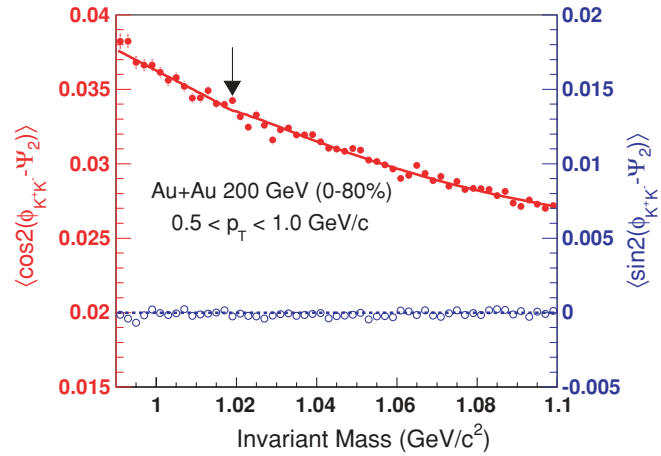

FIG. 7. (Color online) $\langle\cos[2(\varphi_{K^+K^-} - \Psi_2)]\rangle$ (full red points) and $\langle\sin[2(\varphi_{K^+K^-} - \Psi_2)]\rangle$ (open blue points) as a function of $m_{\rm inv}$ of K^+K^- pairs at $0.5 < p_T < 1.0$ GeV/c in Au + Au 200 GeV collisions (0–80%), where the solid curve is the result of fitting by Eq. (10). The arrow shows the position of the ϕ invariant mass peak. The dashed line shows the zero horizontal line.

anisotropic flow v_n of a short-lived particle from that of all possible daughter pairs as a function of invariant mass. For extracting the v_2 of the ϕ meson, it utilizes the fact that the v_2 of K^+K^- pairs is composed of the v_2 of the combinatorial background and the v_2 of the ϕ meson. Following the mixed-event background-subtraction procedure described in Sec. II D, the number of K^+K^- pairs in each invariant-mass bin were counted, irrespective of the pair azimuth. Then

$$N_{K^+K^-}(m_{\rm inv}) = N_\phi(m_{\rm inv}) + N_B(m_{\rm inv}), \qquad (9)$$

where N_ϕ and N_B are from the ϕ signal and the background, respectively. Once N_ϕ has been extracted via event-mixing and fitting the ϕ mass peak with Eq. (3) for each p_T bin as discussed in Sec. II D, N_B can be obtained from Eq. (9).

The same-event v_2 for K^+K^- pairs vs invariant mass can be described by the function

$$v_2(m_{\rm inv}) = a(m_{\rm inv})v_{2S} + [1 - a(m_{\rm inv})]v_{2B}(m_{\rm inv}), \qquad (10)$$

where $v_2(m_{\rm inv})$ is the v_2 of same-event K^+K^- pairs, $v_{2S} \equiv v_{2\phi}$ is the v_2 of the ϕ meson, v_{2B} is the effective v_2 of the combinatorial background and $a(m_{\rm inv}) = N_\phi(m_{\rm inv})/N_{K^+K^-}(m_{\rm inv})$ is the ratio of the ϕ signal to the sum of the background and ϕ signal. The reaction plane angle Ψ_2 was estimated in the same way as for the reaction plane method described in the previous section. Therefore the two methods are not completely independent. $v_2(m_{\rm inv})$ can then be calculated from the following equation [66] for each $m_{\rm inv}$ bin

$$v_2(m_{\rm inv}) = \langle\cos[2(\varphi_{KK} - \Psi_2)]\rangle, \qquad (11)$$

where φ_{KK} is the azimuthal angle of the K^+K^- pair.

Under the assumption that the background contribution to $v_2(m_{\rm inv})$ [the second part on right side of Eq. (10)] is smooth as a function of $m_{\rm inv}$ [68], a polynomial function, $p_0 + p_1 m_{\rm inv} + p_2 m_{\rm inv}^2$, can be used to parametrize the background v_{2B} vs $m_{\rm inv}$. v_{2S} is then obtained by fitting v_2 by Eq. (10) in each p_T bin, with v_{2S} as a free parameter. Figure 7 shows $\langle\cos[2(\varphi_{K^+K^-} - \Psi_2)]\rangle$ [i.e., v_2 in Eq. (11)] vs $m_{\rm inv}$ for $0.5 < p_T < 1.0$ GeV/c in Au + Au 200 GeV collisions (0–80%), where the solid curve is the result of fitting Eq. (10). At the same time, $\langle\sin[2(\varphi_{K^+K^-} - \Psi_2)]\rangle$ vs $m_{\rm inv}$ (open points) is found, as expected, to be consistent with zero due to collisional geometry symmetry [66]. The v_{2S} value [i.e., $v_2^{\rm obs}$ in Equation (7)] determined by the fit was corrected for the reaction plane resolution to obtain the final v_2 for the ϕ meson. The final v_2 results and related discussions will be presented in Sec. III E.

H. Systematic uncertainties

Major contributions to the systematic uncertainties come from variations in the procedure used for extracting the yields from the K^+K^- invariant mass distributions and from variations in the determination of tracking and particle identification efficiencies. Different residual background functions (first-order vs third-order polynomial curves) were used to estimate the uncertainty of the raw yield extraction in each bin, and it was found to be of the order of ∼4.5%. The uncertainty due to different mixed-event normalization factors was estimated to be ∼2.1% by varying the normalization region in the mixed-event background distribution. The uncertainty from tracking and PID efficiencies was estimated to be ∼8%, by varying the kinematic and PID cuts on the daughter tracks.

The overall systematic uncertainty was estimated to be approximately 10% for the yield (dN/dy), and 10% for $\langle p_T\rangle$ for the Au + Au and d + Au data. It includes an additional contribution from the difference between exponential and Levy function fittings of the transverse mass or transverse momentum distributions. The systematic uncertainty in the overall normalization for the $p + p$ 200 GeV data was found to be 15% for dN/dy and 5% for $\langle p_T\rangle$, including uncertainties due to vertex finding and trigger inefficiency for low multiplicity events.

Systematic uncertainties for the v_2 measurement from the two different v_2 extraction methods show p_T and centrality dependences, which mainly result from the determination of $S/(S+B)$ ratios for the invariant mass method and from the removal of residual background in the reaction plane method, respectively. In our analysis, the point-to-point systematic errors included contributions from the following:

(i) Difference in finding the ϕ-meson signal via bin-by-bin counting or Breit-Wigner function fitting methods;
(ii) Difference due to the residual background fitting function: first- or third-order polynomial functions;
(iii) Difference in combinatorial background determination: rotation of the background (the mixed event is from the azimuthal angle rotation of all tracks from the same event) or event-mixing (the current method);
(iv) Difference in v_2 calculation: centrality-by-centrality v_2 calculation and then weighting to get the final MB v_2 or direct calculation of the v_2 through MB raw yield fitting.

III. RESULTS

A. Mass and width

Figure 8 shows the ϕ invariant mass peak position and width (FWHM) as a function of p_T for Au + Au 200 GeV (0–5%), Au + Au 62.4 GeV (0–20%), d + Au 200 GeV (0–20%), and $p + p$ 200 GeV (NSD) collisions. In the larger p_T region (>1 GeV/c), the measured mass and width for the ϕ meson are consistent with those from Monte Carlo (MC) embedding simulations in various collision systems and at different energies. At low p_T (<1 GeV/c), the measured ϕ meson mass is lower and the width is larger than from simulation. The drop of the ϕ meson mass in both real data and simulation at low p_T is due to the multiple scattering energy loss of low p_T tracks in the detector, which is not fully corrected during track reconstruction.

Figure 9 shows shape comparisons between experimental and MC invariant mass distributions for the ϕ meson at $0.6 < p_T < 1.0$ GeV/c in $p + p$ 200 GeV (NSD) and Au + Au 200 GeV (0–5%) collisions. The real data ϕ invariant mass peak (solid circles) is wider than that from standard MC data set (1) (open circles). If the momentum resolution for low p_T kaons used in the simulations is increased by 50%, e.g., kaon momentum resolution at 350 MeV/c increases from ~2% [MC data set (1)] to ~3% [MC data set (2)], the ϕ meson width from simulation reproduces the measured width from real data as shown by open diamonds. This decreased momentum resolution in MC could be possible considering uncertainties in simulations for the amount of material between the TPC active volume and the primary collision vertex and residual geometry alignment issues. These remaining issues for the differences in mass and width of ϕ mesons between real data and simulations have limited our sensitivity to possible small modifications of ϕ meson properties in the medium produced at RHIC collisions. It should also be noted that to really trace down the possible modification of the ϕ meson mass and width in heavy-ion collisions, measurements through the dilepton decay channel are needed. An interesting excess on the low-mass side of the ϕ meson invariant mass peak was observed by an $e^+ + e^-$ channel in the low $\beta\gamma$ region ($\beta\gamma < 1.25$) for 12 GeV p + Cu interactions from the recent KEK experiment [22,23]. This may indicate a vector meson mass modification at normal nuclear density. ϕ measurements using the dilepton channel

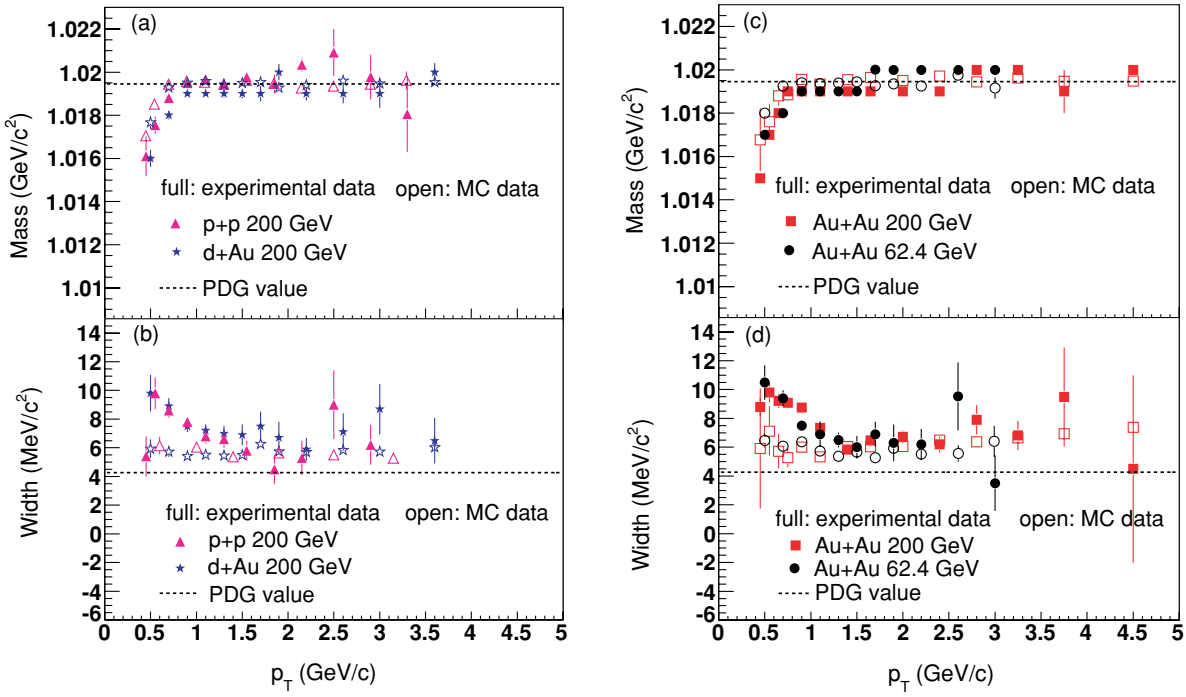

FIG. 8. (Color online) Masses and widths (FWHMs) of ϕ as a function of p_T in $p + p$ 200 GeV (NSD), d + Au 200 GeV (0–20%), Au + Au 62.4 GeV (0–20%), and Au + Au 200 GeV (0–5%) collisions, with the corresponding PDG values.

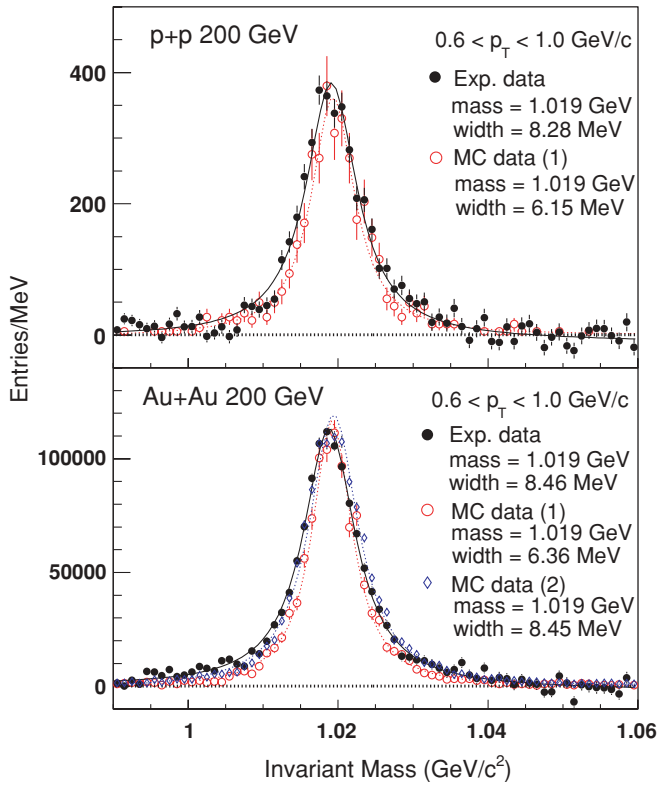

FIG. 9. (Color online) Invariant mass distributions of ϕ meson at $0.6 < p_T < 1.0$ GeV/c in $p + p$ 200 GeV (NSD) and Au + Au 200 GeV (0–5%) collisions. Solid symbols: experimental data. Open symbols: MC simulation. Curves are the results of a Breit-Wigner function fit. Note: Two sets of MC data are shown for Au + Au 200 GeV, and see text for details.

will hopefully be addressed in STAR in year 2010 with the time-of-flight detector upgrade under construction.

B. Spectra

ϕ meson differential invariant yields were calculated by correcting the extracted raw yield by tracking efficiency, detector acceptance, and the decay branching ratio. Figure 10 shows the ϕ meson transverse mass ($m_T = \sqrt{p_T^2 + m_0^2}$, where m_0 is the mass of ϕ meson) distributions from Au + Au collisions at $\sqrt{s_{NN}} = 62.4$, 130, and 200 GeV and from $p + p$ (NSD) and d + Au collisions at $\sqrt{s_{NN}} = 200$ GeV. All spectra are from midrapidity, $|y| < 0.5$, with p_T coverage above 0.4 GeV/c. For clarity, distributions for different centralities are scaled by factors indicated in the figure. Lines in the figure represent fits to the transverse mass distributions for different centralities. The 62.4, 130, and 200 GeV Au + Au data were fitted by the exponential function

$$\frac{1}{2\pi m_T}\frac{d^2N}{dm_T\,dy} = \frac{dN/dy}{2\pi T_{\rm exp}(m_0 + T_{\rm exp})}e^{-(m_T - m_0)/T_{\rm exp}}, \quad (12)$$

where the slope parameter $T_{\rm exp}$ and yield dN/dy are free parameters. For the $p + p$ 200 GeV and d + Au 200 GeV data, the distributions were fitted by a Levy function [69,70], i.e.,

$$\frac{1}{2\pi m_T}\frac{d^2N}{dm_T dy} = \frac{dN/dy(n-1)(n-2)}{2\pi n T_{\rm Levy}(nT_{\rm Levy} + m_0(n-2))} \times \left(1 + \frac{m_T - m_0}{nT_{\rm Levy}}\right)^{-n}, \quad (13)$$

where n, the slope parameter $T_{\rm Levy}$, and yield dN/dy are free parameters. For the four most peripheral centrality bins (40–50%, 50–60%, 60–70%, and 70–80%) in Au + Au collisions at 200 GeV, the distributions were better fit by a Levy than by an exponential function. In fact, the exponential function [Eq. (12)] is the limit of the Levy function [Eq. (13)] as n approaches infinity; i.e., $T_{\rm exp} = T_{\rm Levy}$ ($n \to \infty$). Table III lists the extracted slope parameter T, mean transverse momentum $\langle p_T \rangle$, and yield dN/dy from the best fits to the spectra. Overall estimated systematic uncertainties on these quantities are also listed.

The ϕ meson transverse mass spectra in central Au + Au collisions can be well described by a single m_T-exponential function, while the spectra in d + Au, $p + p$, and peripheral Au + Au are better described by a Levy function, due to the power-law tail at intermediate and high p_T. Figure 11 compares the transverse momentum spectra shapes in different 200 GeV collision systems (0–5% Au + Au, 0–20% d + Au, and inelastic $p + p$). The spectra are normalized by the number of binary collisions ($N_{\rm bin}$) and number of participant pairs ($N_{\rm part}/2$). $N_{\rm bin}$ and $N_{\rm part}$ were determined by Glauber model calculations [56]. We again point out that STAR only triggered on NSD $p + p$ events (measured $\sigma_{\rm NSD} = 30.0 \pm 3.5$ mb) [71], while the Glauber model calculations use the $p + p$ inelastic cross section ($\sigma_{\rm inel} = 42 \pm 1.0$ mb). Thus the NSD $p + p$ spectrum was normalized to the inelastic yield by a correction factor of 30/42.

A change in the shape of spectra from $p + p$, d + Au, and peripheral Au + Au collisions to central Au + Au collisions is clearly visible. In comparison with the fitting result for 200 GeV $p + p$ collisions in the high p_T ($4.0 < p_T < 6.0$ GeV/c) region, the $N_{\rm bin}$ normalized yield is suppressed in central Au + Au collisions at 200 GeV, while no suppression is observed for d + Au collisions at 200 GeV. Since particles with high transverse momentum are mostly produced in hard scattering processes and modified by interactions with the medium in high energy heavy-ion collisions [72–74], the change of ϕ spectra from the Levy function shape in peripheral Au + Au collisions to an exponential function shape in central Au + Au collisions may indicate that different physics dominates the particle production in this p_T region. In the low p_T ($p_T < 1.0$ GeV/c) region, the $N_{\rm part}/2$ normalized ϕ yield in d + Au collisions scales with that in $p + p$ collisions, whereas it is enhanced significantly in central Au + Au collisions. This indicates that the hot environment created by central Au + Au collisions favors the production of soft ϕ mesons.

Theoretical calculations have shown that particles with different transverse momenta (or in different collision

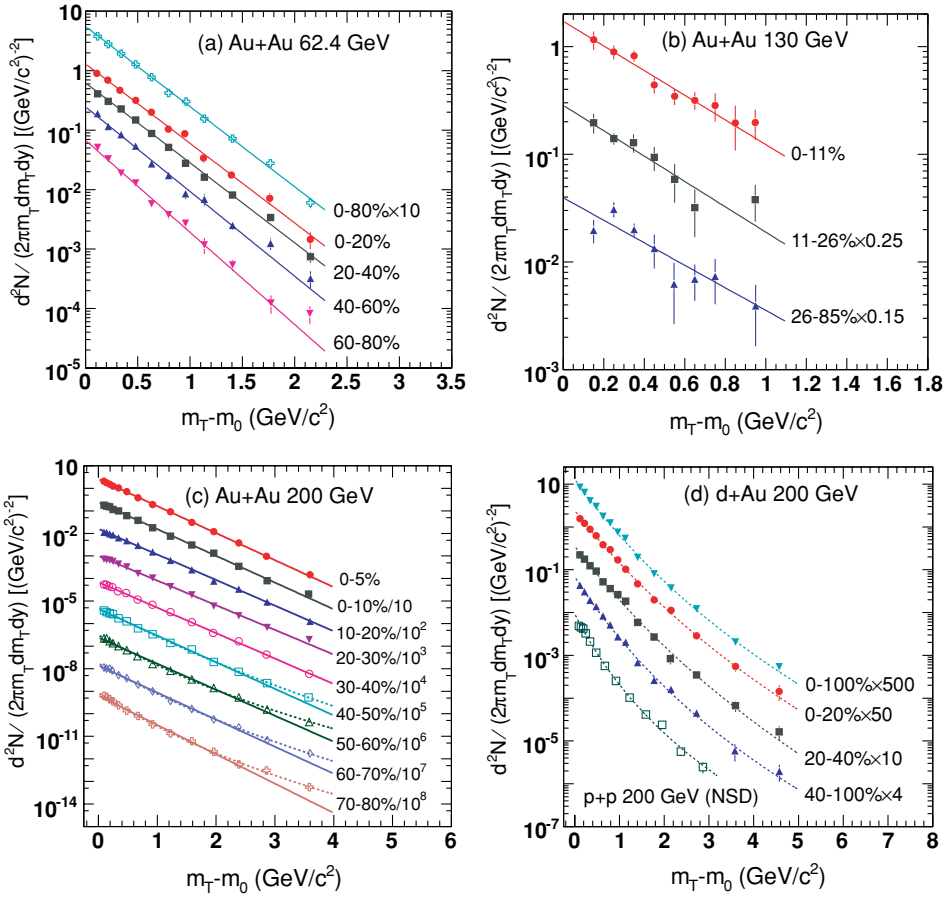

FIG. 10. (Color online) ϕ meson transverse mass distributions for different collision systems and different energies. For clarity, distributions for some centrality bins have been scaled by factors indicated in the figure. Curves represent the exponential (solid) and Levy (dashed) function fits to the distributions. Error bars are statistical only. Note that a scale factor of 1.09 is applied to the ϕ meson spectra for Au + Au collisions at 200 GeV in Ref. [50] to correct for the kaon identification efficiency effect missed previously.

systems) are produced by or evolve with different mechanisms, such as hydrodynamics [35–38], coalescence/recombination [39–44], fragmentation [75–77] and jet quenching [72–74] mechanisms. The observed change of the ϕ p_T spectra shape in our measurements is likely due to the change of these production mechanisms in different kinematic regions and collision systems. Further evidence of this will be discussed later, based on the measurements of different observables.

Figure 12 presents the ϕ meson midrapidity yield per participant pair $(dN/dy)/(0.5N_{\rm part})$ as a function of $N_{\rm part}$ (approximately proportional to the size of the collision system). The measured midrapidity yield per participant pair increases nonlinearly with $N_{\rm part}$, except for the largest centrality bins and the Au + Au 130 GeV results where there are only three centrality bins with big error bars due to the limited statistics. For 200 GeV collisions, the yield increases rapidly from $p + p$ and d + Au to peripheral Au + Au collisions and then saturates for midcentral Au + Au collisions. For the same $N_{\rm part}$, $(dN/dy)/0.5N_{\rm part}$ increases with the collision energy of the Au + Au collisions. This is expected because of the increase of energy available to produce the ϕ mesons. The centrality and energy dependences of the enhancement of ϕ meson production can reflect the mechanism of strangeness enhancement in a dense medium formed in high energy heavy-ion collisions [78].

The upper panel of Fig. 13 shows the $N_{\rm part}$ dependence of ϕ meson $\langle p_T \rangle$ in different collision systems, where $\langle p_T \rangle$ is extracted from the best fit to the m_T spectra as described and shown in Table III. The measured $\langle p_T \rangle$ of the ϕ meson shows no significant centrality dependence within systematic errors. At the same $N_{\rm part}$ value, the ϕ meson $\langle p_T \rangle$ increases slightly with collision energy from 62.4 to 200 GeV.

The mean values of transverse momentum $\langle p_T \rangle$ as a function of hadron mass from 62.4 and 200 GeV central Au + Au collisions are presented in the lower panel of Fig. 13. These data are taken from Refs. [30,79]. The $\langle p_T \rangle$ of ordinary hadrons π^-, K^-, and $\bar{p}$ follows a trend that is increasing with the mass of the hadron, as expected from the dynamics of these particles coming from a common radial velocity field shown as the hatched band [Hydro. model (1)] in the plot [80,81]. However, heavy hyperons such as Ξ and Ω show a deviation from the trend. Their values of $\langle p_T \rangle$ are lower than the expected ones. The observed $\langle p_T \rangle$ values for ϕ meson and Λ are similar to those of Ξ and Ω. Meanwhile, another hydrodynamic model (2) shown by the curve [82,83], which considers possible different chemical freeze-out temperatures for ordinary and strange hadrons, gives a better description for strange particle $\langle p_T \rangle$. This behavior can be explained if strange hadrons have a smaller scattering cross section than ordinary hadrons in the later hadronic stage of the collisions. These strange particles would then decouple earlier from the system. The collective motion of the ϕ meson and multistrange hadrons Ξ and Ω should have been developed at the early partonic stage in Au + Au collisions at RHIC. If radial flow is built up through the evolution of the system, the

TABLE III. Results from fits to the transverse mass distributions of the ϕ meson. The fit functions used to extract the results are also listed. All values are for midrapidity $|y| < 0.5$. The first error is statistical; the second is systematic.

	Centrality	Fit function	χ^2/ndf	$T_{\mathrm{exp/Levy}}$ (MeV)	n	$\langle p_T \rangle$ (MeV/c)	dN/dy
Au + Au	0–20%	Exp.	8.4/9	$328 \pm 6 \pm 22$	–	$922 \pm 13 \pm 61$	$3.52 \pm 0.08 \pm 0.45$
(62.4 GeV)	20–40%	Exp.	8.4/9	$324 \pm 6 \pm 23$	–	$913 \pm 12 \pm 65$	$1.59 \pm 0.03 \pm 0.15$
	40–60%	Exp.	14.5/9	$308 \pm 8 \pm 25$	–	$881 \pm 16 \pm 71$	$0.58 \pm 0.01 \pm 0.07$
	60–80%	Exp.	13.3/9	$279 \pm 9 \pm 28$	–	$822 \pm 19 \pm 82$	$0.15 \pm 0.004 \pm 0.02$
Au + Au	0–11%	Exp.	5.3/7	$379 \pm 50 \pm 45$	–	$1095 \pm 147 \pm 131$	$5.73 \pm 0.37 \pm 0.57$
(130 GeV [49])	11–26%	Exp.	3.2/5	$369 \pm 73 \pm 44$	–	$1001 \pm 144 \pm 120$	$3.33 \pm 0.38 \pm 0.33$
	26–85%	Exp.	9.0/6	$417 \pm 75 \pm 50$	–	$1021 \pm 99 \pm 123$	$0.98 \pm 0.12 \pm 0.10$
Au + Au	0–5%	Exp.	11.0/12	$357 \pm 3 \pm 23$	–	$977 \pm 7 \pm 64$	$7.95 \pm 0.11 \pm 0.73$
(200 GeV)	0–10%	Exp.	10.2/12	$359 \pm 5 \pm 24$	–	$979 \pm 20 \pm 66$	$7.42 \pm 0.14 \pm 0.68$
	10–20%	Exp.	9.7/12	$373 \pm 4 \pm 26$	–	$1010 \pm 8 \pm 69$	$5.37 \pm 0.09 \pm 0.50$
	20–30%	Exp.	26.7/12	$387 \pm 4 \pm 26$	–	$1022 \pm 14 \pm 68$	$3.47 \pm 0.06 \pm 0.44$
	30–40%	Exp.	21.1/12	$371 \pm 4 \pm 24$	–	$1005 \pm 8 \pm 64$	$2.29 \pm 0.04 \pm 0.23$
	40–50%	Levy	17.4/11	$315 \pm 11 \pm 38$	22.7 ± 4.3	$949 \pm 13 \pm 67$	$1.44 \pm 0.03 \pm 0.14$
	50–60%	Levy	6.9/11	$290 \pm 13 \pm 34$	13.8 ± 1.9	$955 \pm 14 \pm 87$	$0.82 \pm 0.02 \pm 0.09$
	60–70%	Levy	7.4/11	$291 \pm 13 \pm 29$	18.6 ± 3.6	$926 \pm 15 \pm 75$	$0.45 \pm 0.01 \pm 0.05$
	70–80%	Levy	5.5/11	$243 \pm 15 \pm 25$	13.0 ± 2.3	$851 \pm 19 \pm 85$	$0.20 \pm 0.01 \pm 0.02$
$p + p$ (200 GeV, NSD [14])	0–100%	Levy	10.1/10	$202 \pm 14 \pm 11$	8.3 ± 1.2	$812 \pm 30 \pm 41$	$0.018 \pm 0.001 \pm 0.003$
d + Au	0–20%	Levy	4.7/11	$323 \pm 20 \pm 32$	15.5 ± 3.9	$1030 \pm 57 \pm 103$	$0.146 \pm 0.005 \pm 0.014$
(200 GeV)	20–40%	Levy	13.6/11	$316 \pm 19 \pm 32$	16.9 ± 4.7	$1007 \pm 35 \pm 101$	$0.103 \pm 0.003 \pm 0.010$
	40–100%	Levy	12.4/11	$263 \pm 15 \pm 26$	12.2 ± 2.1	$920 \pm 35 \pm 92$	$0.040 \pm 0.001 \pm 0.004$
	0–100% (MB)	Levy	17.5/11	$297 \pm 11 \pm 30$	13.9 ± 1.8	$973 \pm 26 \pm 97$	$0.071 \pm 0.001 \pm 0.005$

particles with a smaller hadronic cross section would have smaller radial velocity and relatively smaller $\langle p_T \rangle$.

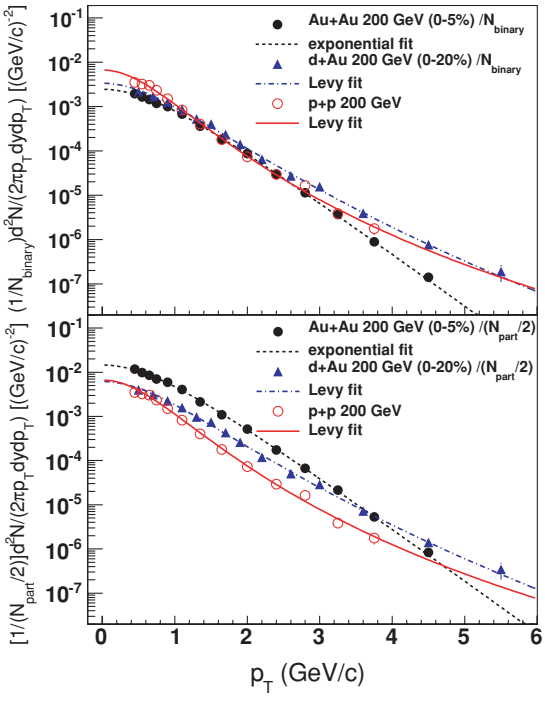

FIG. 11. (Color online) Comparison of transverse momentum spectra shape among different 200 GeV collision systems: Au + Au (0–5%), d + Au (0–20%), and $p + p$ (inelastic). The spectra are normalized by N_{bin} (top panel) and $N_{\mathrm{part}}/2$ (bottom panel).

C. Ratios

The yield ratio ϕ/π^- as a function of the center-of-mass energy per nucleon pair ($\sqrt{s_{NN}}$) is presented in the upper panel of Fig. 14. The ϕ/π^- ratio increases with energy in both $A + A$ [14,30,49,84–86] and $p + p$ collisions [87–90], indicating that the yield of the ϕ increases faster than that of the π^- in $A + A$ and $p + p$ collisions with increasing $\sqrt{s_{NN}}$. The ϕ/π^- ratio in $A + A$ collisions is enhanced compared to that for $p + p$ collisions, which indicates that $A + A$ collisions may provide a more advantageous environment for the production of ϕ mesons. In fact, an enhanced production of

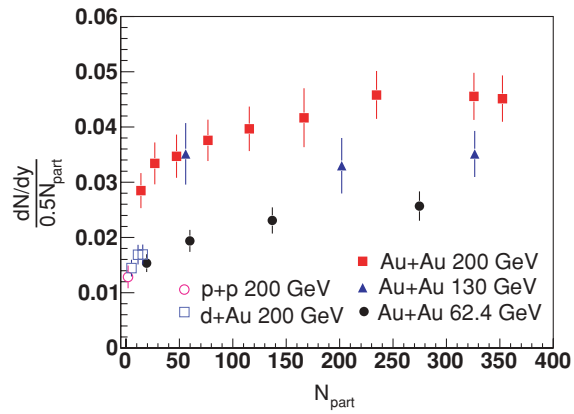

FIG. 12. (Color online) N_{part} dependence of $(dN/dy)/0.5N_{\mathrm{part}}$ in five different collision systems: Au + Au 62.4, 130, 200 GeV; $p + p$ 200 GeV (inelastic); and d + Au 200 GeV. Statistical and systematic errors are included.

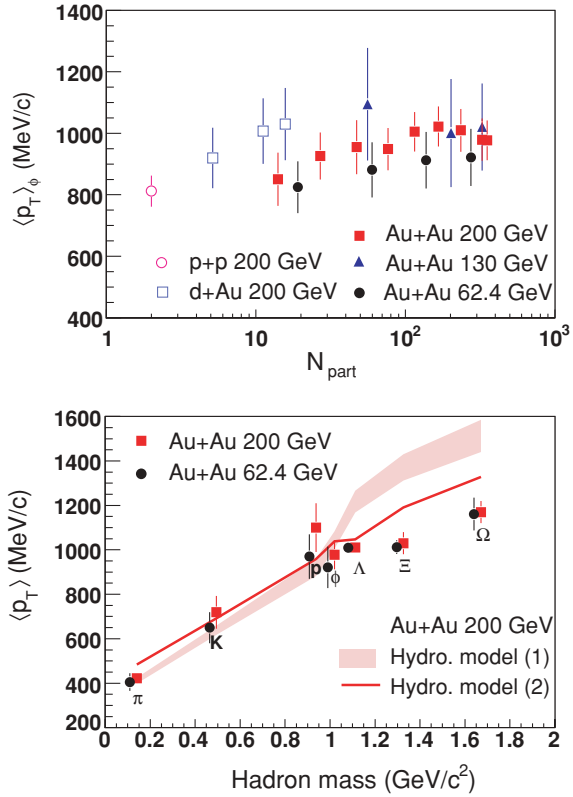

FIG. 13. (Color online) Top panel: $N_{\rm part}$ dependence of $\langle p_T \rangle_\phi$ in different collision systems. Bottom panel: Hadron mass dependence of $\langle p_T \rangle$ in central Au + Au collisions at 62.4 and 200 GeV. The band and curve show two hydrodynamic model calculations for central Au + Au collisions at 200 GeV. Note: Hadron masses for the Au + Au 62.4 GeV data are shifted slightly in the x-axis direction for clarity, and systematic errors are included for ϕ.

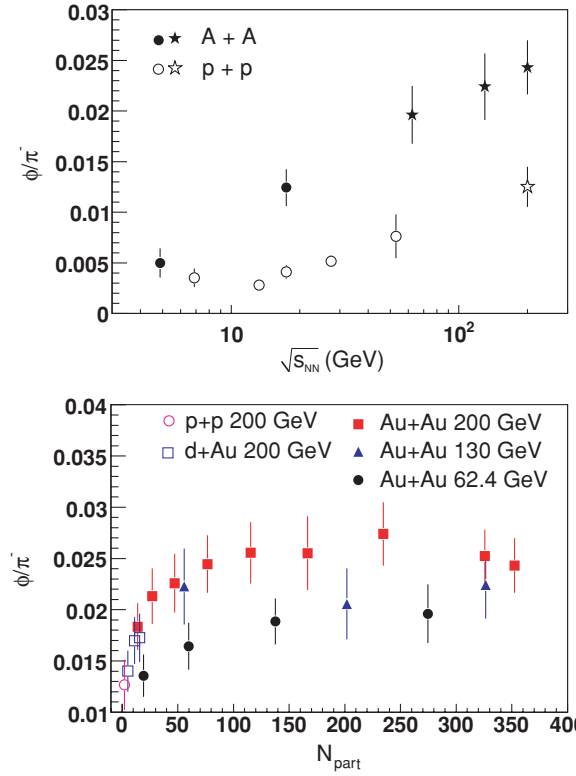

FIG. 14. (Color online) Top panel: Energy dependence of the ratio ϕ/π^- in $A + A$ (full points) and $p + p$ (open points) collisions. Stars are data from the STAR experiment at RHIC. Bottom panel: $N_{\rm part}$ dependence of ratio ϕ/π^- in different collision systems. Systematic errors are included for the STAR data points.

ϕ meson in a heavy-ion environment has been predicted to be a signal of QGP formation [5]. However, no clear conclusion can be drawn from the experimental measurements, since the relative enhancement from $p + p$ to $A + A$ collisions does not seem to change for $\sqrt{s_{NN}} > 10$ GeV. The bottom panel of Fig. 14 shows the $N_{\rm part}$ dependence of the ϕ/π^- ratio in different collisions. The ϕ/π^- ratio first increases with $N_{\rm part}$, and then seems to be saturated in the high $N_{\rm part}$ region.

To further study whether ϕ meson production, or just that of strange particles, is enhanced in high energy $A + A$ collisions with respect to elementary collisions, we have plotted the yield ratio of ϕ/K^- as a function of $\sqrt{s_{NN}}$ in $A + A$, $e + e$, and $p + p$ collisions in the top panel of Fig. 15. For these collisions, at energies above the threshold for ϕ production, the ϕ/K^- ratio is essentially independent of collision species and energy from a few GeV up to 200 GeV [14,30,49,84–90]. The lower panel of Fig. 15 shows that the yield ratio ϕ/K^- from our analysis is also almost constant as a function of centrality. This is remarkable considering that the environment created by $p + p$ collisions is so drastically different from that of Au + Au collisions that have both partonic and hadronic interactions.

The centrality dependence of the ϕ/K^- ratio provides another serious test for rescattering models based on the assumption that kaon coalescence is the dominant mechanism for ϕ production. The $K\bar{K}$ and K-hyperon modes are included in these rescattering models [12,13]. They predict an increasing ϕ/K^- ratio vs centrality (shown by the dashed line in the lower panel of Fig. 15), which is again in contradiction with the approximately flat trend of our measurements. Note also that the ϕ/K^- ratio from the UrQMD model is scaled by a factor of 3.4 to match the magnitude of our measurement for peripheral Au + Au collisions. The comparisons of the data to predictions from these rescattering models including $\langle p_T \rangle$ and ϕ/K^- effectively rule out kaon coalescence as the dominant production mechanism for the ϕ meson. These measurements of the ϕ/K^- ratio may point to a common underlying production mechanism for ϕ and strange mesons in all collision systems.

In addition, statistical models [91–95] based on the assumption that the accessible phase space is fully saturated and thermalized can reproduce the STAR measurements of integrated hadron yield ratios (including ϕ/π^- and ϕ/K^-) at midrapidity in $p + p$ and Au + Au collisions at 200 GeV [34]. In these statistical models, the strangeness phase-space occupancy factor γ_s approaches unity with increasing $N_{\rm part}$, which indicates that strangeness approaches/reaches chemical equilibration for midcentral and central Au + Au collisions at RHIC energies.

Because the mechanisms of (multi)strange particle production are predicted to be very sensitive to the early phase of

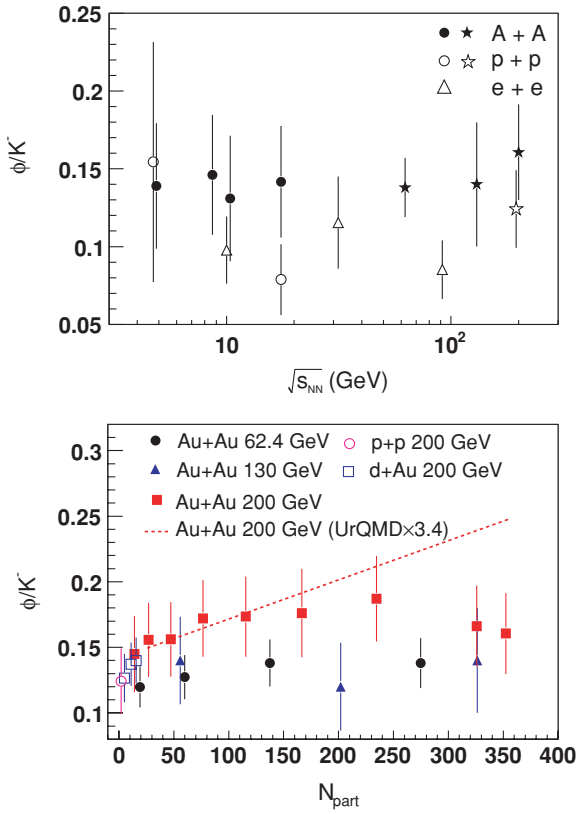

FIG. 15. (Color online) Top panel: Energy dependence of ratio ϕ/K^- in $A + A$ and elementary ($e + e$ and $p + p$) collisions. Stars are data from STAR experiments at RHIC. Bottom panel: N_{part} dependence of ratio ϕ/K^- in different collision systems. The dashed line shows results from UrQMD model calculations. Systematic errors are included for the STAR data points.

nuclear collisions, the ratio of Ω/ϕ is expected to reflect the partonic nature of the thermal source that characterizes QGP [96] and the effects of the strong color field (SCF) [98]. In Fig. 16, the ratios of Ω/ϕ vs p_T are presented for different

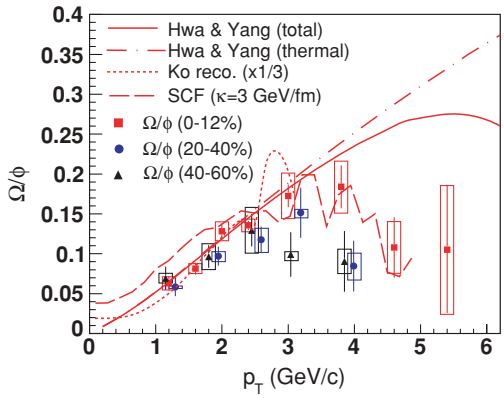

FIG. 16. (Color online) The Ω/ϕ ratio vs p_T for three centrality bins in $\sqrt{s_{NN}} = 200$ GeV $Au + Au$ collisions, where the data points for 40–60% are shifted slightly for clarity. As shown in the legend, the lines represent results from Hwa and Yang [96], Ko *et al.* [97], and, for SCF, Refs. [98,99].

centrality bins. The Ω ($\Omega^- + \overline{\Omega}^+$) data points are from Ref. [34] (for 0–12%) and from Ref. [100] for the other centralities. Also shown in the figure are three curves from two recombination model expectations for central collisions. A model by Ko *et al.*, based on the dynamical recombination of quarks [97], is compared with the data and found to overpredict the ratio by a factor of about 3 over the whole p_T region. (Note: the bumpy shape for this model is due to the limited statistics of their Monte Carlo simulation of the model.) Based on ϕ and Ω production from coalescence of thermal s quarks in the medium [96], Hwa and Yang can describe the trend of the data up to $p_T \sim 4$ GeV/c but fail at higher p_T (solid line). In the alternative SCF scenario [98,99], a large string tension of $\kappa = 3$ GeV/fm can reproduce the data up to $p_T \sim 4.5$ GeV/c in the framework of the HIJING/$B\overline{B}$ v2.0 model, but the effect of strong color electric fields remains an open issue and needs to be further investigated. With decreasing centrality, the observed Ω/ϕ ratios seem to turn over at successively lower values of p_T, possibly indicating a smaller contribution from thermal quark coalescence in more peripheral collisions [96]. This is also reflected in the smooth evolution of the p_T spectra shapes from the thermal-like exponentials to Levy-like curves.

D. Nuclear modification factor

The measurement of the nuclear modification factors R_{cp} and R_{AB} provides a sensitive tool to probe the production dynamics and hadronization process in relativistic heavy-ion collisions [39–44]. R_{cp}, which is the ratio of yields in central to peripheral heavy-ion collisions normalized by N_{bin}, is defined as

$$R_{\text{cp}}(p_T) = \frac{[dN/(N_{\text{bin}}dp_T)]^{\text{central}}}{[dN/(N_{\text{bin}}dp_T)]^{\text{peripheral}}}, \tag{14}$$

and R_{AB}, which is the yield ratio of nucleus (A) + nucleus (B) collisions to inelastic $p + p$ collisions normalized by N_{bin}, is defined as

$$R_{AB}(p_T) = \frac{[dN/(N_{\text{bin}}dp_T)]^{A+B}}{[dN/dp_T]^{p+p}}, \tag{15}$$

where N_{bin} is the number of binary inelastic nucleon-nucleon collisions determined from Glauber model calculations [71,101]. It is obvious that these two ratios will be unity if nucleus-nucleus collisions are just simple superpositions of nucleon-nucleon collisions. Deviation of these ratios from unity would imply contributions from nuclear or QGP effects. It should be mentioned that when using $p + p$ collisions in the R_{AB} ratio, inelastic collisions should be used instead of the measured NSD collisions, therefore a correction factor 30/42, which was discussed in the above subsection B, was applied to correct the NSD yield to the inelastic yield in $p + p$ collisions. There is a p_T-dependent correction to the NSD distribution from singly diffractive (SD) events, which is small in our measured p_T range, being 1.05 at $p_T = 0.4$ GeV/c and unity above 1.2 GeV/c as determined from PYTHIA simulations [71].

Figure 17 presents the p_T dependence of R_{cp} for the ϕ with respect to midperipheral (top panel) and most-peripheral (bottom panel) bins in $Au + Au$ collisions at 200 GeV. Results

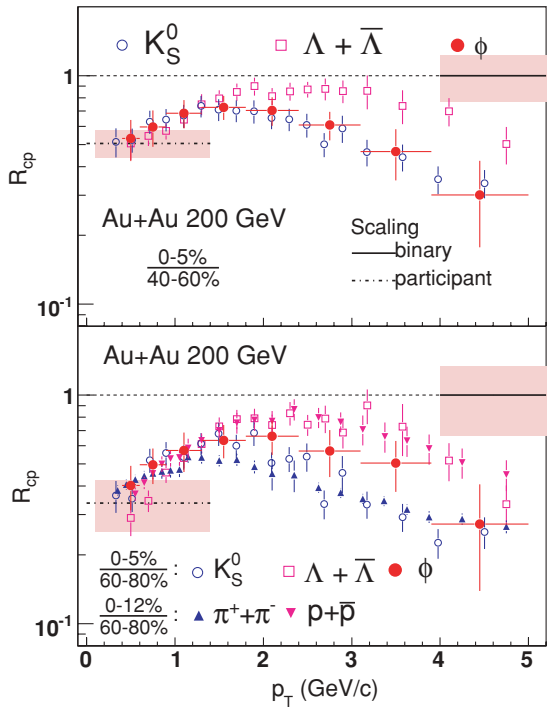

FIG. 17. (Color online) p_T dependence of the nuclear modification factor R_{cp} in Au + Au 200 GeV collisions. The top and bottom panels present R_{cp} from midperipheral and most-peripheral collisions, respectively. See legend for symbol and line designations. The rectangular bands show the uncertainties of binary and participant scalings. Statistical and systematic errors are included.

for the $\Lambda + \bar{\Lambda}$, the K^0_S [45], the $\pi^+ + \pi^-$, and the $p + \bar{p}$ [102] particles are also shown in the figure for comparison. Both statistical and systematic errors are included. Most of the systematic errors cancel in the ratios; however, the uncertainty due to particle identification from dE/dx remains as the dominant source and varies from point to point over the range ~7%–12%. In the measured p_T region, the R_{cp} of ϕ meson is consistent with N_{part} scaling at lowest p_T (dot-dashed line), and is significantly suppressed relative to the binary collision scale (dashed horizontal line at unity) at all p_T in Au + Au collisions at 200 GeV. When compared to the STAR measured $\Lambda + \bar{\Lambda}$ and K^0_S data [45], the R_{cp} for ϕ follows that of K^0_S rather than that of the similarly massive Λ ($\bar{\Lambda}$), especially for the case of 0–5%/40–60%. For 0–5%/60–80%, the R_{cp} of ϕ sits between that for the K^0_S and the Λ. This may be attributed to the shape change of the ϕ spectra from exponential at 40–60% centrality to Levy at 60–80% centrality as discussed above, which may be due to the change of the ϕ production mechanism at intermediate p_T in different environments with different degrees of strangeness equilibration.

Figure 18 presents the p_T dependence of R_{cp} for the ϕ meson for Au + Au 62.4 and 200 GeV and d + Au 200 GeV collisions. For the three collision systems, the R_{cp} factor follows N_{part} scaling at low p_T. However, the R_{cp} at intermediate p_T is strongly suppressed in Au + Au collisions at 200 GeV, is weakly suppressed in Au + Au collisions at 62.4 GeV, and shows no suppression in d + Au collisions at 200 GeV.

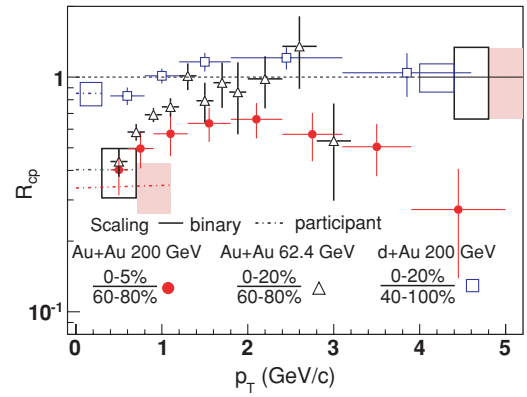

FIG. 18. (Color online) p_T dependence of the nuclear modification factor R_{cp} in Au + Au 62.4 and 200 GeV and d + Au 200 GeV collisions, where rectangular bands represent the uncertainties of binary and participant scalings (see legend). Statistical and systematic errors are included.

Our measured R_{cp} for the ϕ meson further supports the proposed partonic coalescence/recombination scenario at intermediate p_T [42,43,47,48], where the centrality dependence of particle yield depends on the number of constituent quarks (NCQ) rather than on the mass of the particle. Das and Hwa [47] proposed a recombination scenario to explain the leading particle effect in $p + p$ collisions, where the fragmenting partons would recombine with sea quarks to form hadrons. The resulting p_T distribution for the leading particle is therefore determined by the fragmenting quarks. In heavy-ion collisions, it is possible that $q\bar{q}$ (qqq) come together and form a meson (baryon) due to the high density of quarks (antiquarks) in the collision system. The abundant nearby partons give the recombination/coalescence mechanism a comparative advantage over the fragmentation mechanism for particle production in the intermediate p_T region, and this successfully explains the relative enhancement of baryons in the intermediate p_T region, such as the ratios p/π and Λ/K^0_S [102–104]. Recently, Hwa and Yang used their recombination model to successfully describe the ϕ meson p_T spectra, but it fails to reproduce the p_T dependence of Ω/ϕ at higher p_T as shown in the previous subsection. They assumed that for the production of ϕ this thermal component dominates over others involving jet shower contributions because of the suppression of shower s quarks in central Au + Au collisions [96]. However, the partonic medium, with an intrinsic temperature, may modify the recombination probability and momentum distribution for the ϕ [42,43,48].

Figure 19 presents the p_T dependence of the nuclear modification factor R_{AB} in Au + Au and d + Au collisions at 200 GeV. For comparison, data points for $R_{d\mathrm{Au}}$ of $\pi^+ + \pi^-$ and $p + \bar{p}$ are also shown in the figure. The $R_{d\mathrm{Au}}$ of ϕ mesons reveals a similar enhancement trend as those of $\pi^+ + \pi^-$ and $p + \bar{p}$ at the intermediate p_T, which was attributed to be the Cronin effect [105–107]. The Cronin enhancement may result either from momentum broadening due to multiple soft [108] (or semihard [109–112]) scattering in the initial state or from final state interactions suggested in the recombination model [113]. These mechanisms lead to different particle type

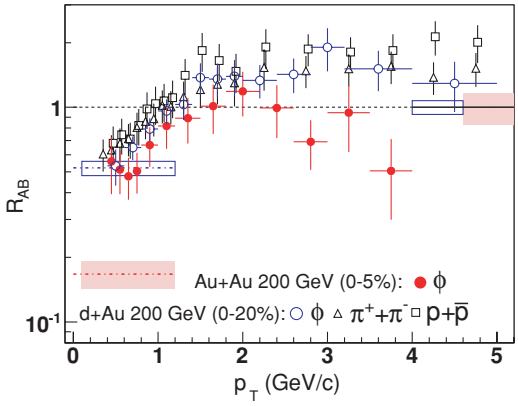

FIG. 19. (Color online) p_T dependence of the nuclear modification factor R_{AB} for ϕ in Au + Au 200 GeV and d + Au 200 GeV collisions. For comparison, data points for $\pi^+ + \pi^-$ in d + Au 200 GeV and $p + \bar{p}$ in d + Au 200 GeV are also shown (see legend). Rectangular bands show the uncertainties of binary (solid line) and participant (dot-dash line) scalings. Systematic errors are included for ϕ, $\pi^+ + \pi^-$, and $p + \bar{p}$.

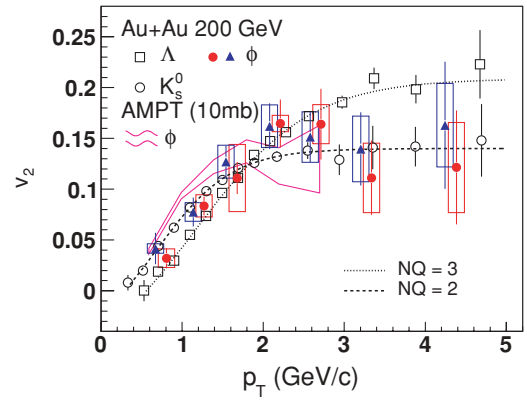

FIG. 20. (Color online) p_T dependence of the elliptic flow v_2 of ϕ, Λ, and K^0_S in Au + Au collisions (0–80%) at 200 GeV. Data points for ϕ are from the reaction plane method (full up-triangles) and invariant mass method (full circles), where data points from the reaction plane method are shifted slightly along the x axis for clarity. Vertical error bars represent statistical errors, while the square bands represent systematic uncertainties. The magenta curved band represents the v_2 of the ϕ meson from the AMPT model with a string melting mechanism [116]. The dash and dot curves represent parametrizations inspired by number-of-quark scaling ideas from Ref. [117] for NQ = 2 and NQ = 3, respectively.

and/or mass dependence in the nuclear modification factors as a function of p_T. Our measurement of $R_{d\mathrm{Au}}$ of ϕ mesons does not have the precision to differentiate particle dependence scenarios [114,115]. On the other hand, the R_{AA} in Au + Au 200 GeV is lower than that in d + Au 200 GeV and consistent with the binary collision scaling at intermediate p_T. These features are consistent with the scenario that features the onset of parton-medium final state interactions in Au + Au collisions. The two R_{AB} observations in central d + Au and Au + Au collisions are consistent with the shape comparisons in Fig. 11 (top panel).

E. Elliptic flow

Figure 20 shows the elliptic flow v_2 of the ϕ meson as a function of p_T in MB (0–80%) Au + Au collisions at $\sqrt{s_{NN}} = 200$ GeV. The v_2 of the K^0_S and Λ measured by STAR [45] in Au + Au 200 GeV collisions are also shown for comparison. Measurements of v_2 for the ϕ meson from both reaction plane and invariant mass methods are presented, and they are consistent with each other.

The first interesting observation is that the ϕ meson has significantly nonzero v_2 in the measured p_T region. If the ϕ meson has a small interaction cross section with the evolving hot-dense matter in $A + A$ collisions, it would not participate in the late-stage hadronic interactions in contrast to hadrons such as π, K, and $p(\bar{p})$ which freeze-out later. This indicates that the nonzero v_2 of the ϕ meson must have been developed in the earlier partonic stage. In the low p_T region (<2 GeV/c), the v_2 value of ϕ is between that for the K^0_S and the Λ in Au + Au 200 GeV collisions, consistent with the expectation of a mass ordering for v_2 in hydrodynamic models. These observations support the hypothesis of the development of partonic collectivity and possible thermalization in the early stages of heavy-ion collisions at RHIC [34,100], although the underlying mechanism for the equilibration process remains an open issue.

In the intermediate p_T region (~2–5 GeV/c), the v_2 of the ϕ meson is consistent with that for the K^0_S rather than for the Λ. When we fit the $v_2(p_T)$ of ϕ mesons with the quark number scaling function [117], the resulting fit parameter NCQ (number of constitute quarks) = 2.3 ± 0.4. The fact that the $v_2(p_T)$ of ϕ is the same as that of other mesons indicates that the heavier s quarks flow as strongly as the lighter u and d quarks. The AMPT model with string melting and parton coalescence mechanisms can reproduce the experimental results well up to 3 GeV/c, which favors the hadronization scenario of coalescence/recombination of quarks [116,118].

The v_2 of the ϕ meson from other centralities are shown in Fig. 21. The data are analyzed from the invariant mass

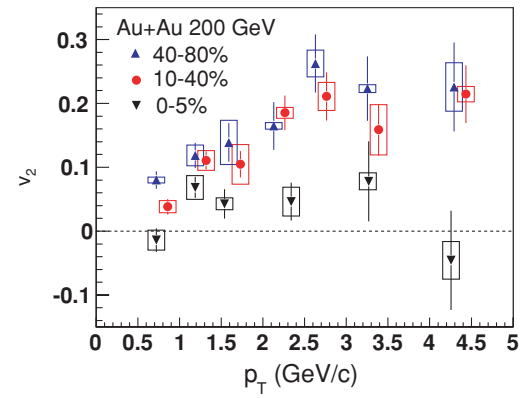

FIG. 21. (Color online) Elliptic flow v_2 as a function of p_T, $v_2(p_T)$, for the ϕ meson from different centralities. The vertical error bars represent the statistical errors, while the square bands represent the systematic uncertainties. For clarity, data points of 10–40% are shifted in the p_T direction slightly.

TABLE IV. Integrated elliptic flow $\langle v_2 \rangle$ for the ϕ meson for four centrality bins in Au + Au collisions at 200 GeV.

Centrality (%)	$\langle v_2 \rangle$ (%)
40–80	$8.5 \pm 1.1(\text{stat}) \pm 0.2(\text{sys})$
10–40	$6.6 \pm 0.8(\text{stat}) \pm 0.2(\text{sys})$
0–5	$2.1 \pm 1.2(\text{stat}) \pm 0.5(\text{sys})$
0–80	$5.8 \pm 0.6(\text{stat}) \pm 0.2(\text{sys})$

method only. As expected, $v_2(p_T)$ increases with increasing eccentricity (decreasing centrality) of the initial overlap region. This trend is also illustrated in Table IV, which presents the p_T-integrated values of ϕ-meson elliptic flow, $\langle v_2 \rangle$, calculated by convoluting the $v_2(p_T)$ with the respective p_T spectrum for four centrality bins. It should be noted that the centrality dependence of the $\langle v_2 \rangle$ of the ϕ meson is consistent with that of the charged hadrons [67].

IV. CONCLUSION

In conclusion, STAR has measured ϕ meson production for 62.4, 130, 200 GeV Au + Au, 200 GeV d + Au, and NSD $p + p$ collisions at RHIC. Details of the analysis method for ϕ meson are presented. The respective energy and N_{part} dependence of the ϕ meson production, as well as the p_T spectra for five collision systems, are reported.

The ϕ spectra in central Au + Au 200 GeV collisions are described well by an exponential function. The spectra for $p + p$, d + Au, and the most peripheral Au + Au 200 GeV collisions are better described by a Levy function due to the high-p_T power-law tails. This change of spectra shape from $p + p$, d + Au, and peripheral Au + Au to central Au + Au collisions is most likely due to a change of the dominant ϕ production mechanism in the different collision environments. The yield of ϕ mesons per participant pair increases and saturates with the increase of N_{part}. It is found that the $\langle p_T \rangle$ of ϕ, Λ, Ξ, and Ω does not follow the $\langle p_T \rangle$ vs hadron mass trend determined by the π^-, K^-, and $\bar{p}$. This may be due to their small hadronic cross sections, which indicates that the ϕ and strange hadrons can retain more information about the early state of the collision system.

The ϕ/K^- yield ratios from $p + p$ and $A + B$ collisions over a broad range of collision energies above the ϕ threshold are remarkably close to each other, indicating similar underlying hadronization processes for soft strange quark pairs in these collisions. The lack of a significant centrality dependence of the ϕ/K^- yield ratio and $\langle p_T \rangle_\phi$ effectively rules out kaon coalescence as a dominant production channel at RHIC. The trend of the Ω/ϕ ratio is consistent with recombination models and a strong color field scenario up to $p_T \sim 4$ GeV/c in central Au + Au collisions.

The measurement of the ϕ meson nuclear modification factor R_{AB} is consistent with the Cronin effect in d + Au 200 GeV collisions, and with the energy loss mechanism in Au + Au 200 GeV collisions. The ϕ meson was found to have nonzero v_2 in the measured p_T range. When comparing the ϕ meson nuclear modification factor R_{cp} (0–5%/40–60%) and elliptic flow v_2 to those of the similar mass Λ baryon, and to the lighter K^0_S meson, we see that the ϕ meson clearly behaves more like the K^0_S meson than the Λ baryon. Therefore, the processes relevant to R_{cp} and v_2 at intermediate p_T are driven not by the mass of the particle, but rather by the type of the particle, i.e., number of constituent quarks (NCQ) scaling. The coalescence/recombination model provides a fairly consistent picture to describe particle production in the intermediate p_T region over a broad range of collision energies and system sizes at RHIC.

ACKNOWLEDGMENTS

We thank the RHIC Operations Group and RCF at BNL, the NERSC Center at LBNL, and the resources provided by the Open Science Grid consortium for their support. This work was supported in part by the Offices of NP and HEP within the US DOE Office of Science, the US NSF, the Sloan Foundation, the DFG Excellence Cluster EXC153 of Germany, CNRS/IN2P3, RA, RPL, and EMN of France, STFC and EPSRC of the United Kingdom, FAPESP of Brazil, the Russian Ministry of Sci. and Tech., the NNSFC, CAS, MoST, and MoE of China, IRP and GA of the Czech Republic, FOM of the Netherlands, DAE, DST, and CSIR of the Government of India, Swiss NSF, the Polish State Committee for Scientific Research, and the Korea Sci. & Eng. Foundation.

[1] L. Bertanza *et al.*, Phys. Rev. Lett. **9**, 180 (1962).
[2] S. Okubo, Phys. Lett. **5**, 165 (1963).
[3] G. Zweig, CERN Report Nos. TH-401 and TH-412, 1964 (unpublished).
[4] J. Iizuka, K. Okada, and O. Shito, Prog. Theor. Phys. **35**, 1061 (1966).
[5] A. Shor, Phys. Rev. Lett. **54**, 1122 (1985).
[6] J. Rafelski and B. Muller, Phys. Rev. Lett. **48**, 1066 (1982).
[7] J. Rafelski, Nucl. Phys. **A418**, 215c (1984).
[8] M. Jacob and J. Tran Thanh Van, Phys. Rep. **88**, 321 (1982).
[9] P. Koch and J. Rafelski, Nucl. Phys. **A444**, 678 (1985).
[10] A. J. Baltz and C. Dover, Phys. Rev. C **53**, 362 (1996).
[11] H. Sorge *et al.*, Phys. Lett. **B289**, 6 (1992).
[12] H. Sorge, Phys. Rev. C **52**, 3291 (1995).
[13] M. Bleicher *et al.*, J. Phys. G **25**, 1859 (1999).
[14] J. Adams *et al.* (STAR Collaboration), Phys. Lett. **B612**, 181 (2005).
[15] K. H. Ackermann *et al.* (STAR Collaboration), Nucl. Instrum. Methods A **499**, 624 (2003).
[16] M. Asakawa and C. M. Ko, Nucl. Phys. **A572**, 732 (1994).
[17] C. Song, Phys. Lett. **B388**, 141 (1996).
[18] M. Asakawa and C. M. Ko, Phys. Lett. **B322**, 33 (1994).
[19] K. Haglin, Nucl. Phys. **A584**, 719 (1995).
[20] W. Smith and K. L. Haglin, Phys. Rev. C **57**, 1449 (1998).
[21] C. M. Ko and D. Seibert, Phys. Rev. C **49**, 2198 (1994).
[22] R. Muto *et al.*, Phys. Rev. Lett. **98**, 042501 (2007).

[23] F. Sakuma *et al.*, Phys. Rev. Lett. **98**, 152302 (2007).
[24] L. Alvarez-Ruso and V. Koch, Phys. Rev. C **65**, 054901 (2002).
[25] T. Ishikawa *et al.*, Phys. Lett. **B608**, 215 (2005).
[26] H. J. Behrend *et al.*, Phys. Lett. **B56**, 408 (1975).
[27] A. Sibirtsev, H. W. Hammer, U. G. Meissner, and A. W. Thomas, Eur. Phys. J. A **29**, 209 (2006).
[28] P. Lévai and B. Müller, Phys. Rev. Lett. **67**, 1519 (1991).
[29] H. Stöcker, Nucl. Phys. **A750**, 121 (2005).
[30] J. Adams *et al.* (STAR Collaboration), Phys. Rev. Lett. **92**, 112301 (2004).
[31] C. Adler *et al.* (STAR Collaboration), Phys. Rev. Lett. **87**, 182301 (2001).
[32] S. S. Adler *et al.* (PHENIX Collaboration), Phys. Rev. Lett. **91**, 182301 (2003).
[33] C. Adler *et al.* (STAR Collaboration), Phys. Rev. Lett. **89**, 132301 (2002).
[34] J. Adams *et al.* (STAR Collaboration), Nucl. Phys. **A757**, 102 (2005).
[35] J.-Y. Ollitrault, Phys. Rev. D **46**, 229 (1992).
[36] H. Sorge, Phys. Rev. Lett. **82**, 2048 (1999).
[37] P. Huovinen *et al.*, Phys. Lett. **B503**, 58 (2001).
[38] D. Teaney, J. Lauret, and E. V. Shuryak, Phys. Rev. Lett. **86**, 4783 (2001).
[39] Z.-W. Lin and C. M. Ko, Phys. Rev. Lett. **89**, 202302 (2002).
[40] S. A. Voloshin, Nucl. Phys. **A715**, 379 (2003).
[41] V. Greco, C. M. Ko, and P. Lévai, Phys. Rev. Lett. **90**, 202302 (2003).
[42] R. J. Fries, B. Muller, C. Nonaka, and S. A. Bass, Phys. Rev. Lett. **90**, 202303 (2003).
[43] R. J. Fries, B. Muller, C. Nonaka, and S. A. Bass, Phys. Rev. C **68**, 044902 (2003).
[44] D. Molnar and S. A. Voloshin, Phys. Rev. Lett. **91**, 092301 (2003).
[45] J. Adams *et al.* (STAR Collaboration), Phys. Rev. Lett. **92**, 052302 (2004).
[46] J. Adams *et al.* (STAR Collaboration), Phys. Rev. C **71**, 064902 (2005).
[47] K. P. Das and R. C. Hwa, Phys. Lett. **B68**, 459 (1977).
[48] R. C. Hwa and C. B. Yang, Phys. Rev. C **67**, 064902 (2003).
[49] C. Adler *et al.* (STAR Collaboration), Phys. Rev. C **65**, 041901 (2002).
[50] B. I. Abelev *et al.* (STAR Collaboration), Phys. Rev. Lett. **99**, 112301 (2007).
[51] S. Blyth, Ph.D. thesis, Cape Town University, 2007, http://drupal.star.bnl.gov/STAR/files/startheses/2007/blyth_sarah.ps.
[52] M. Anderson *et al.* (STAR Collaboration), Nucl. Instrum. Methods A **499**, 659 (2003).
[53] K. H. Ackermann *et al.* (STAR Collaboration), Nucl. Instrum. Methods A **499**, 713 (2003).
[54] F. S. Bieser *et al.* (STAR Collaboration), Nucl. Instrum. Methods A **499**, 766 (2003).
[55] C. Adler *et al.* (STAR Collaboration), Nucl. Instrum. Methods A **499**, 433 (2003).
[56] B. I. Abelev *et al.* (STAR Collaboration), Phys. Rev. C **79**, 034909 (2009).
[57] W.-M. Yao *et al.* (Particle Data Group), J. Phys. G **33**, 1 (2006).
[58] H. Bichsel, Nucl. Instrum. Methods A **562**, 154 (2006).
[59] D. L'Hote, Nucl. Instrum. Methods A **337**, 544 (1994).
[60] D. Drijard, H. G. Fischer, and T. Nakada, Nucl. Instrum. Methods A **225**, 367 (1984).
[61] E. Yamamoto, Ph.D. thesis, University of California-Los Angeles, 2001, http://drupal.star.bnl.gov/STAR/files/startheses/2001/yamamoto_eugene.pdf.
[62] F. Carminati *et al.*, GEANT 3.21: Detector Description 38 and Simulation Tool, CERN Program Library Long Writeup W5013, 1993 (unpublished).
[63] J. Adams *et al.* (STAR Collaboration), Phys. Lett. **B637**, 161 (2006).
[64] J. Ma, Ph.D. thesis, University of California-Los Angeles, 2006, http://drupal.star.bnl.gov/STAR/files/startheses/2006/ma_jingguo.pdf.
[65] K. H. Ackermann *et al.* (STAR Collaboration), Phys. Rev. Lett. **86**, 402 (2001).
[66] A. M. Poskanzer and S. A. Voloshin, Phys. Rev. C **58**, 1671 (1998).
[67] J. Adams *et al.* (STAR Collaboration), Phys. Rev. C **72**, 014904 (2005).
[68] N. Borghini and J. Y. Ollitrault, Phys. Rev. C **70**, 064905 (2004).
[69] G. Wilk and Z. Wlodarczyk, Phys. Rev. Lett. **84**, 2770 (2000).
[70] J. Adams *et al.* (STAR Collaboration), Phys. Rev. C **71**, 064902 (2005).
[71] J. Adams *et al.* (STAR Collaboration), Phys. Rev. Lett. **91**, 172302 (2003).
[72] M. Gyulassy and M. Plumer, Phys. Lett. **B243**, 432 (1990).
[73] X.-N. Wang and M. Gyulassy, Phys. Rev. D **44**, 3501 (1991).
[74] X.-N. Wang and M. Gyulassy, Phys. Rev. Lett. **68**, 1480 (1992).
[75] T. Sjostrand, arXiv:hep-ph/9508391.
[76] B. Andersson *et al.*, arXiv:hep-ph/0212122.
[77] B. A. Kniehl *et al.*, Nucl. Phys. **B597**, 337 (2001).
[78] B. I. Abelev *et al.*, Phys. Lett. **B673**, 183 (2009).
[79] B. I. Abelev *et al.* (STAR Collaboration), Phys. Rev. Lett. **97**, 132301 (2006).
[80] P. F. Kolb and R. Rapp, Phys. Rev. C **67**, 044903 (2003).
[81] N. Xu, Nucl. Phys. **A787**, 44c (2007).
[82] O. Socolowski, F. Grassi, Y. Hama, and T. Kodama, Phys. Rev. Lett. **93**, 182301 (2004).
[83] W.-L. Qian *et al.*, arXiv:0709.0845.
[84] K. Adcox *et al.* (PHENIX Collaboration), Phys. Rev. Lett. **88**, 242301 (2002).
[85] B. B. Back *et al.* (E917 Collaboration), Phys. Rev. C **69**, 054901 (2004).
[86] S. V. Afanasiev *et al.* (NA49 Collaboration), Phys. Lett. **B491**, 59 (2000).
[87] V. Blobel *et al.*, Phys. Lett. **B59**, 88 (1975).
[88] C. Daum *et al.* (ACCMOR Collaboration), Nucl. Phys. **B186**, 205 (1981).
[89] M. Aguilar-Benitez *et al.*, Z. Phys. C **50**, 405 (1991).
[90] D. Drijard *et al.*, Z. Phys. C **9**, 293 (1981).
[91] G. D. Yen *et al.*, Phys. Rev. C **56**, 2210 (1997).
[92] S. Wheaton and J. Cleymans, Comput. Phys. Commun. **180**, 84 (2009).
[93] P. Braun-Munzinger *et al.*, Phys. Lett. **B344**, 43 (1995).
[94] P. Braun-Munzinger *et al.*, Phys. Lett. **B365**, 1 (1996).
[95] P. Braun-Munzinger, I. Heppe, and J. Stachel, Phys. Lett. **B465**, 15 (1999).
[96] R. C. Hwa and C. B. Yang, Phys. Rev. C **75**, 054904 (2007).
[97] L.-W. Chen and C. M. Ko, Phys. Rev. C **73**, 044903 (2006).
[98] V. Topor Pop, M. Gyulassy, J. Barrette, C. Gale, S. Jeon, and R. Bellwied, Phys. Rev. C **75**, 014904 (2007).
[99] N. Armesto *et al.*, J. Phys. G: Nucl. Part. Phys. **35**, 054001 (2008).

[100] J. Adams *et al.* (STAR Collaboration), Phys. Rev. Lett. **98**, 062301 (2007).
[101] J. Adams *et al.* (STAR Collaboration), arXiv:nucl-ex/0311017.
[102] B. I. Abelev *et al.* (STAR Collaboration), Phys. Rev. Lett. **97**, 152301 (2006).
[103] J. Adams *et al.* (STAR Collaboration), arXiv:nucl-ex/0601042.
[104] B. I. Abelev *et al.* (STAR Collaboration), Phys. Lett. **B655**, 104 (2007).
[105] J. W. Cronin *et al.*, Phys. Rev. D **11**, 3105 (1975).
[106] D. Antreasyan, J. W. Cronin, H. J. Frisch, M. J. Shochet, L. Kluberg, P. A. Piroue, and R. L. Sumner, Phys. Rev. D **19**, 764 (1979).
[107] P. B. Straub *et al.*, Phys. Rev. Lett. **68**, 452 (1992).
[108] M. Lev and B. Petersson, Z. Phys. C **21**, 155 (1983).
[109] A. Accardi and M. Gyulassy, Phys. Lett. **B586**, 244 (2004).
[110] G. Papp, P. Lévai, and G. I. Fai, Phys. Rev. C **61**, 021902(R) (1999).
[111] I. Vitev and M. Gyulassy, Phys. Rev. Lett. **89**, 252301 (2002).
[112] X.-N. Wang, Phys. Rev. C **61**, 064910 (2000).
[113] R. C. Hwa and C. B. Yang, Phys. Rev. Lett. **93**, 082302 (2004).
[114] R. C. Hwa, C. B. Yang, and R. J. Fries, Phys. Rev. C **71**, 024902 (2005).
[115] B. I. Abelev *et al.* (STAR Collaboration), Phys. Rev. C **76**, 054903 (2007).
[116] J. H. Chen *et al.*, Phys. Rev. C **74**, 064902 (2006).
[117] X. Dong *et al.*, Phys. Lett. **B597**, 328 (2004).
[118] Z.-W. Lin, C. M. Ko, B. A. Li, B. Zhang, and S. Pal, Phys. Rev. C **72**, 064901 (2005).